Universität Stuttgart

Geodätisches Institut

GRAIL Lunar Gravity Field Recovery Simulations Based on Short-Arc Analysis

Master Thesis

GEOENGINE

an der Universität Stuttgart

Wenjian Qin

Stuttgart, September 2012

Betreuer: Dr. Oliver Baur
Österreichische Akademie der Wissenschaften

Dr. Tilo Reubelt
Universität Stuttgart

Prof. Dr.-Ing. Nico Sneeuw
Universität Stuttgart

Erklärung der Urheberschaft

Ich erkläre hiermit an Eides statt, dass ich die vorliegende Arbeit ohne Hilfe Dritter und ohne Benutzung anderer als der angegebenen Hilfsmittel angefertigt habe; die aus fremden Quellen direkt oder indirekt übernommenen Gedanken sind als solche kenntlich gemacht. Die Arbeit wurde bisher in gleicher oder ähnlicher Form in keiner anderen Prüfungsbehörde vorgelegt und auch noch nicht veröffentlicht.

Ort, Datum Unterschrift

Acknowledgement

First I would like to show my deepest gratitude to my supervisor, Dr. Oliver Baur, who offered me such a great opportunity to study and work at the Austrian Academy of Science in Graz with an outstanding group. I really appreciate every effort he has made to help with my living and study there. I learned a lot from his rigorous attitude towards the scientific work. His remarkable patience is gratefully acknowledged.

I also sincerely thank Prof. Nico Sneeuw to totally support my decision to go to Graz. Appreciation goes to Dr. Tilo Reubelt who provided his initial code and simulation data. Additionally, his comments on my thesis are highly appreciated. I am grateful to Dr. Matthias Weigelt who answered my questions and guided my study.

I owe my gratitude to Prof. Wolfgang Keller to arrange F2Geos to provide me with a financial support, which was a guarantee and motivation for my study and life in Graz.

Last but not least, I appreciate every happy or tough time spending with my colleagues from the GEOENGINE program and PhD fellows at the Institute of Geodesy in Stuttgart. I want to dedicate this thesis to my parents, who always have been supporting and encouraging me. I hope I make them proud.

Abstract

The Moon is a fascinating planet with a great importance to planetary science. Due to the lack of geological activities on the Moon, it keeps the historical record of the early Solar System. The knowledge gained from the evolution of the Moon can be extended to other planets.

The Gravity Recovery and Interior Laboratory (GRAIL) mission is the lunar analog of the successful terrestrial Gravity Recovery and Climate Experiment (GRACE) mission to unlock secrets of the Moon. It will provide data to derive the global lunar gravity field with a vast improvement on both the near side and the far side by the implementation of low-low satellite-to-satellite tracking (ll-SST) principle.

Global gravity field recovery aims at deriving the spherical harmonic coefficients to represent the gravitational potential. In this thesis, the short-arc approach is applied and discussed for GRAIL simulation studies.

Key Words: GRAIL, satellite-to-satellite tracking, short-arc analysis, gravity field, Moon.

Contents

List of Figures

List of Tables

Chapter 1

Introduction

1.1 Motivation for lunar gravity field recovery

The Moon is the only natural satellite of the Earth. As our closest neighbor in the Solar System, the Moon is significant to planetary science. This is because the Moon keeps the historical record of the Solar System due to the lack of geological activities on the Moon. The knowledge gained from the evolution of the Moon could be extended to other planets. Therefore, the Moon offers an opportunity to reconstruct the early history of the Solar System.

The Moon has been studied extensively in the long human history. In the past few decades, with the application of satellite techniques, many satellite missions have been successfully set up for various lunar scientific purposes. One of the greatest milestones is United States' National Aeronautics and Space Administration (NASA) Apollo program, which made six manned lunar landings between 1969 and 1972. The Moon became the only celestial body on which humans have set foot besides the Earth.

One of the key problems of lunar research is to understand the evolution of the Moon by determining its interior structure, which calls for the knowledge of the lunar gravity field. The first investigation of the lunar gravity dates back to 1966 by the Soviet spacecraft Luna-10 (Akim, 1967). It was followed by the discovery of mass concentrations (mascons) under the lunar ringed maria by Muller and Sjogren (1968). Moreover, mascons had been proved to be of immense practical importance during the Apollo missions in the late 1960s and early 1970s (Floberghagen, 2001).

Data collected from the recent lunar missions (Table 1.1) have been successfully utilized to obtain the lunar gravity field. The Clementine mission was the first to provide a relatively high resolution of the lunar gravity field (Lemoine et al., 1997). Coming after it was the Lunar Prospector (LP) mission that placed the spacecraft in a low polar circular orbit for the first time. A significant improvement on the nearside gravity field was achieved (Konopliv et al., 2001). The farside gravity field was improved from the tracking data of the Japanese Selenological and Engineering Explorer (SELENE) mission (Namiki et al., 2009). The tracking data of the Chinese Chang'e-1 mission contributed to the lunar gravity field solution in medium and low degree coefficients

(Yan et al., 2010). The first Indian planetary exploration mission Chandrayaan-1 aimed at carrying out high resolution remote sensing studies of the Moon (Goswami and Annadurai, 2009). The Lunar Reconnaissance Orbiter (LRO) mission was designed to undertake a global and detailed survey of the Moon to prepare for the future lunar exploration activities (Chin et al., 2007; Mazarico et al., 2012).

Table 1.1: *Recent lunar missions*

Date	Mission	Country
1994	Clementine	USA
1998	Lunar Prospector	USA
2007	SELENE (Kaguya)	Japan
2007	Chang'e 1	China
2008	Chandrayaan 1	India
2009	LRO	USA
2011	GRAIL	USA

Due to the fact that the Moon and the Earth are in a spin-orbit resonance, the Moon always faces the same side towards the Earth. By the continuous tracking of the spacecraft with the Deep Space Network (DSN), a high resolution of the nearside gravity field can be obtained. However, the farside tracking data are not available since the spacecraft is not in view from the Earth. The method of regularisation is necessary to solve this problem. Most lunar gravity models use information in the form of a Kaula rule to fit the gravity field over the far side (Kaula, 1966). The choice of the regularisation parameter was suggested by Floberghagen (2002). A significant change to this situation is only expected when global satellite-to-satellite tracking data of high quality become available (Floberghagen et al., 1996). For the first time ever, ll-SST is realized with the GRAIL mission to recover the lunar gravity field. As a consequence, GRAIL will provide a much better nearside and a vastly improved farside lunar gravity field (Hoffman et al., 2010).

1.2 Concepts of ll-SST

In the model of ll-SST, two spacecraft are placed in the similar low polar orbits with a separation of up to a few hundreds of kilometers. The relative motion of the two spacecraft varies in space depending on the roughness of the gravity field features. The change of the relative motion is precisely measured by K-band ranging (KBR) system and the orbits are continuously tracked.

This model has been successfully realized for the GRACE mission (Tapley et al., 2004). The global gravity field is obtained from the inter-satellite KBR measurements (range, range-rate and range-acceleration) and the continuous tracking data of the orbit by the Global Positioning System (GPS). This concept can be transferred from GRACE to GRAIL with some proper adjustments.

The solution strategies of ll-SST aim at deriving the gravity field parameters from the KBR measurements and orbit analysis. One solution strategy to establish this connection is achieved by using in-situ observations. In this case all observations are used as in-situ measurements that are linearly related to the gravity field parameters (Han, 2003). Requiring no integration of the equations of motion makes it a more direct approach. The limitation is that it combines highly precise KBR observations with comparably low accurate orbits in one equation. (Weigelt and Keller, 2011). Only by means of dynamic orbits with high accuracy this combination works. Approaches based on in-situ observations include energy integral approach (Han, 2003; Weigelt, 2007), acceleration approach (Austen and Grafarend, 2004; Novák et al., 2006) and LoS gradiometry approach (Keller and Sharifi, 2005).

Another selection is obtained from the numerical integration of the variational equations. Defining the orbits and the KBR measurements as observations directly in the observation equation is one of the advantages, but it also leads to a high computational effort. The classical approach to derive the gravity field parameters is based on this strategy (Reigber, 1989; Tapley et al., 2004). Another one is the short-arc approach that was first proposed as a general method for orbit determination by Schneider (1968) and refined by Mayer-Gürr (2006). The physical model of the short-arc approach is based on Newton's equation of motion, formulated as boundary value problem in the form of a Fredholm-type integral equation. The analysis based on the short-arc approach is discussed in this thesis.

1.3 Thesis objective and outline

The main objective of the thesis is to assess the GRAIL performance by means of a series of closed-loop simulation studies. These studies can basically be divided into two parts, synthesis and analysis. Synthesis covers the simulation of GRAIL observables based on priori gravity field simulation, whereas analysis deals with the recovery of these input parameters from the synthesis data.

In more detail, synthesis includes:

- Simulation of the GRAIL orbit by orbit integration
- Simulation of ll-SST observables
- Formulation of error models for both the orbit and the ll-SST component

Analysis includes:

- Formulation of the ll-SST functional model (according to GRACE experience)
- Inversion of the gravity field parameters from the simulated data

- Quality assessment of GRAIL gravity field determination dependent on error models.

Outline:

Chapter 2 is an overview of the GRAIL mission.

Chapter 3 introduces the fundamentals.

Chapter 4 discusses the gravity field recovery strategies and the mathematical model of the short-arc approach.

Chapter 5 interprets the results and analyses.

Chapter 6 draws the conclusions.

Chapter 2

GRAIL mission overview

2.1 General information

Launched on Sept. 10, 2011, the GRAIL mission (figure 2.1) is a part of NASA's Discovery Program, led by the Principal Investigator, Dr. Maria T. Zuber of the Massachusetts Institute of Technology (MIT). Two operation teams, the Jet Propulsion Laboratory (JPL) for mission management and the Lockheed Martin Space Systems (LM) for flight operation are cooperating together to support this project.

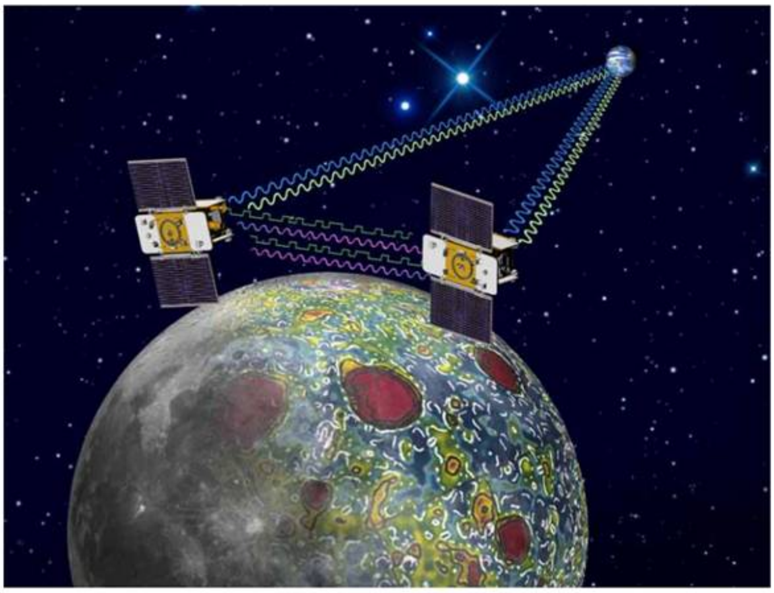

Figure 2.1: *The GRAIL mission (NASA, 2011)*

The GRAIL mission is the lunar analog of the GRACE mission which places two spacecraft into the similar orbits around the Moon. It is the first time ever to employ the ll-SST method in lunar missions. Starting its work in 2012 after a four month low energy trajectory to approach the Moon, the mission will achieve the most accurate gravitational map of the Moon to date.

2.2 Mission design overview

2.2.1 Science objectives

The derived high-resolution gravitational field enables scientists to determine the interior structure and composition of the Moon, from crust to core, to improve the understanding of the thermal evolution (Hoffman et al., 2010). Furthermore, since the history of the Moon represents the history of the early Solar System, the knowledge gained from the Moon could be extended to other planets.

The GRAIL mission consists of six lunar science investigations (Zuber, 2008):

1. Map the structure of the crust and lithosphere.
2. Understand the Moon's asymmetric thermal evolution.
3. Determine the subsurface structure of impact basins and the origin of mascons.
4. Ascertain the temporal evolution of crustal brecciation and magmatism.
5. Constrain deep interior structure from tides.
6. Place limits on the size of the possible inner core.

2.2.2 Orbiter & Payloads

The GRAIL orbiters (figure 2.2) contain two payloads, the Lunar Gravity Ranging System (LGRS) instrument and the Education/Public Outreach (E/PO) instrument.

LGRS is the science payload that includes (Wang and Klipstein, 2010; Beerer and Havens, 2012):

K-band (24 GHz) transmitter-receiver: Measures the relative velocity of the two orbiters.

S-Band (2 GHz) Time Transfer System (TTS): For time correlation between the two orbiters.

X-Band (8 GHz) Ratio Science Beacon (RSB): Provides a one-way X-band signal to the ground for precision orbit determination (POD).

Ultra-Stable Oscillator (USO): Provides a steady reference signal for all data.

The E/PO payload includes (NASA, 2011):

The "MoonKAM[1]" camera: A set of digital cameras operated by middle school students to image the lunar surface under the direction of Sally Ride Science.

[1] Moon Knowledge Acquired by Middle school students

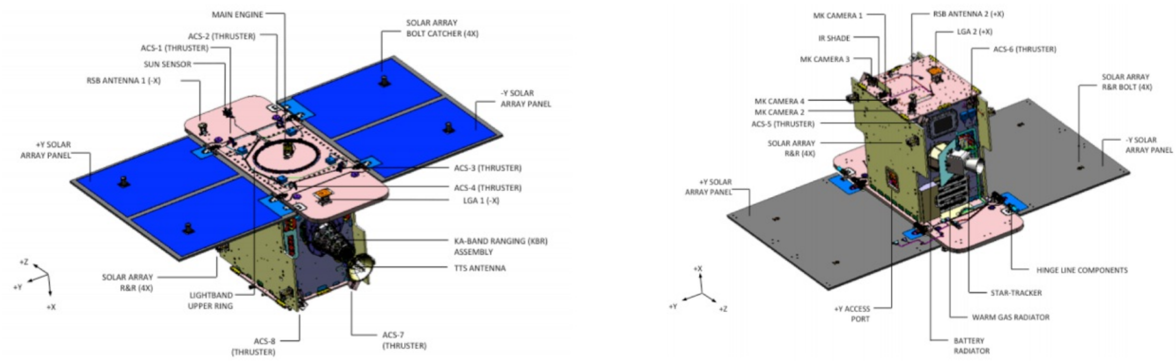

Figure 2.2: GRAIL orbiter view (Beerer and Havens, 2012)

2.2.3 Mission phases

The GRAIL mission consists of eight major mission phases (Hoffman et al., 2010):

Launch Phase: The twin spacecraft were launched in Florida on September 10, 2011 (figure 2.3 shows the prime timeline) on a Delta-II Heavy rocket from the Cape Canaveral Air Force Station (CCAFS).

Trans-lunar Cruise (TLC): The twin spacecraft were in a 108 days low energy trajectory to approach the Moon.

Lunar Orbit Insertion (LOI): Both spacecraft were placed into a near-polar elliptical orbit with an orbit period of 11.5 hours. The two orbiters, GRAIL-A and GRAIL-B, were renamed Ebb and Flow after the insertion.

Orbit Period Reduction (OPR): The orbit period was reduced from 11.5 hours to around 2 hours.

Transition to Science Formation (TSF): A series of maneuvers were established to prepare for the start of data collection.

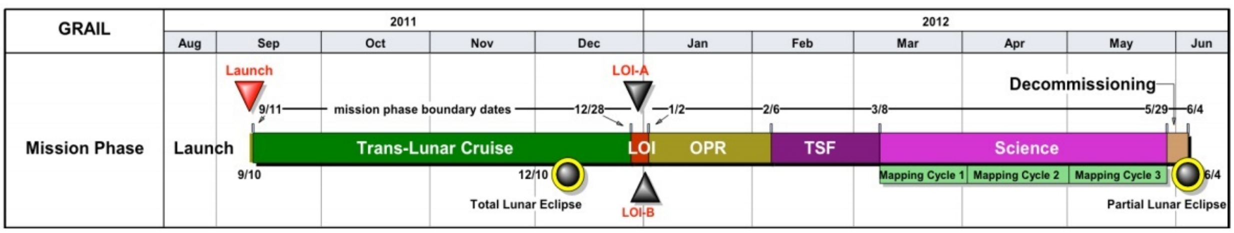

Figure 2.3: GRAIL prime mission timeline (Havens and Beerer, 2012)

Science Phase: The data collection started on March, 1, 2012 (7 days ahead of the schedule). The twin spacecraft completed three 27.3-day (lunar sidereal period) mapping cycles in 82 days. The separation distance of the twin spacecraft varied from 75 km (start of cycle 1) to 216 km (start of cycle 2) and finally decreased to 65 km (end of cycle 3).

Extended mission: The prime GRAIL mission was planned to end at the time of a partial lunar eclipse on June 4, 2012. However, an extended mission was proposed after the analysis from LM showed that the orbiters could survive the lunar eclipse. This enabled GRAIL to obtain another three months data at an even lower orbit from September to November in 2012.

Decommissioning: The orbiters will finally impact the lunar surface after the Extended Mission.

Chapter 3

Fundamentals

This chapter presents the elementary theories that are necessary for gravity field recovery. It starts with the description of two parameterizations in section 3.1.1, followed by the demonstration of transformation equations in section 3.1.2. In section 3.2 the boundary value problem and the Laplace equation solution are explained. The last section deals with Legendre functions.

3.1 Reference systems

Reference systems are essential for modeling the observations for respective purposes in satellite geodesy. It defines the way in which results are interpreted. Some observations obtained in the global geocentric system may have to be processed in the local reference system. This will lead to the transformations between different reference systems.

3.1.1 Parameterization and transformation

Two parameterizations introduced here, Cartesian parameterization and spherical parameterization are two different ways to describe a position in three dimensional space. The choice between these parameterizations depends on how the observations and results are defined.

In a Cartesian parameterization (figure 3.1), the position is defined as x, y and z in three directions. The transformation from one Cartesian system to another Cartesian system can be established through the elementary rotations $\mathbf{R}_1(\alpha)$, $\mathbf{R}_2(\beta)$ and $\mathbf{R}_3(\gamma)$ with respect to three axes.

The transformation from one Cartesian to another Cartesian system is

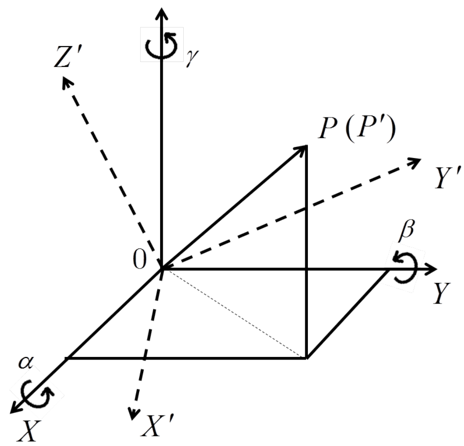

Figure 3.1: *Cartesian coordinates and system rotation*

$$\begin{bmatrix} X'_P \\ Y'_P \\ Z'_P \end{bmatrix} = \underbrace{\mathbf{R}_3(\gamma)\mathbf{R}_2(\beta)\mathbf{R}_1(\alpha)}_{\text{Euler rotation}} \begin{bmatrix} X_P \\ Y_P \\ Z_P \end{bmatrix} \tag{3.1}$$

with the rotation matrices

$$\mathbf{R}_1(\alpha) = \begin{bmatrix} 1 & 0 & 0 \\ 0 & \cos\alpha & \sin\alpha \\ 0 & -\sin\alpha & \cos\alpha \end{bmatrix} \tag{3.2a}$$

$$\mathbf{R}_2(\beta) = \begin{bmatrix} \cos\beta & 0 & -\sin\beta \\ 0 & 1 & 0 \\ \sin\beta & 0 & \cos\beta \end{bmatrix} \tag{3.2b}$$

$$\mathbf{R}_3(\gamma) = \begin{bmatrix} \cos\gamma & \sin\gamma & 0 \\ -\sin\gamma & \cos\gamma & 0 \\ 0 & 0 & 1 \end{bmatrix} \tag{3.2c}$$

In a spherical parameterization (figure 3.2), the position is denoted as r, θ, λ. The transformation between the spherical system and the Cartesian system is

$$\begin{aligned} x &= r\sin\theta\cos\lambda \\ y &= r\sin\theta\sin\lambda \\ z &= r\cos\theta \end{aligned} \tag{3.3}$$

and conversely:

$$
\begin{aligned}
r &= \sqrt{x^2 + y^2 + z^2} \\
\theta &= \arctan \frac{\sqrt{x^2 + y^2}}{z} \\
\lambda &= \arctan \frac{y}{x}
\end{aligned}
\tag{3.4}
$$

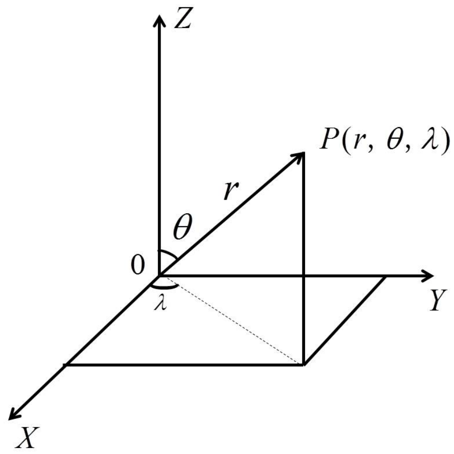

Figure 3.2: *Spherical coordinates*

3.1.2 Conventional reference system

The two parameterizations introduced so far only describe the position in a mathematical way. But the realization of these parameterizations can be on any different frames. This leads to the conception of conventional reference systems.

According to Seeber (2003), a conventional reference system is a system where all models, numerical constants and algorithms are explicitly specified. Two fundamental systems are the conventional inertial reference system (CIS) and the conventional terrestrial reference system (CTS).

CIS is a space-fixed reference system. Newton's equation of motion is only valid in this system. In this frame the satellite motion is usually defined. Since it is an inertial system, extraterrestrial objects are related to this system as well. For this reason, it is also called the celestial reference systems (CRS).

CTS is an earth-fixed reference system ideal for defining the positions of the observation stations and the description of the results in satellite geodesy.

The transformation between CIS and CTS is achieved with the determination of precession, nutation and earth rotation (including polar motion). For the simulation study in this thesis, only the effects coming from the earth rotation, namely the Greenwich

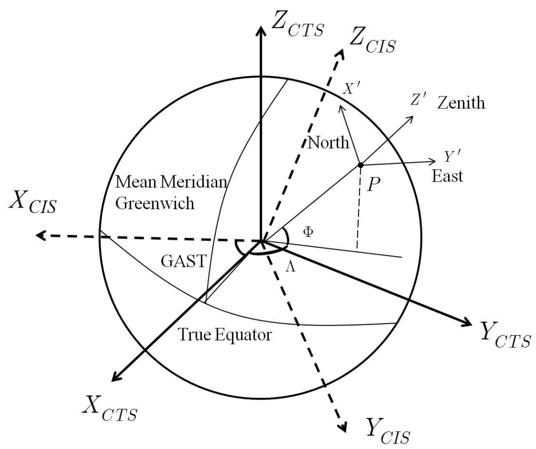

Figure 3.3: *CIS, CTS and local system*

apparent sidereal time (GAST), are took into consideration. To check the full transformation equations including precession, nutation and polar motion, please refer to (Petit and Luzum, 2010).

The transformation between CIS and CTS is

$$\mathbf{X}_{CTS} = \mathbf{R}_3(GAST)\mathbf{X}_{CIS} \tag{3.5}$$

with

$$\mathbf{R}_3(GAST) = \begin{bmatrix} \cos(GAST) & \sin(GAST) & 0 \\ -\sin(GAST) & \cos(GAST) & 0 \\ 0 & 0 & 1 \end{bmatrix} \tag{3.6}$$

The three axes in the local system are oriented toward to North, East and Zenith (figure 3.3). The transformation between CTS and the local system is

$$\mathbf{X}_{CTS} = \mathbf{R}_3(-\Lambda)\mathbf{R}_2(\frac{\pi}{2} + \Phi)\mathbf{X}'_{local} \tag{3.7}$$

with

$$\mathbf{R}_3(-\Lambda)\mathbf{R}_2(\frac{\pi}{2} + \Phi) = \begin{bmatrix} -\sin\Phi\cos\Lambda & -\sin\Lambda & -\cos\Phi\cos\Lambda \\ -\sin\Phi\sin\Lambda & \cos\Lambda & -\cos\Phi\sin\Lambda \\ \cos\Phi & 0 & -\sin\Phi \end{bmatrix} \tag{3.8}$$

3.2 Representation of the gravitational potential

The start point of the gravitational theory is the so called Boundary Value Problem (BVP) (do not confuse with the BVP for the short-arc analysis) which refers to the question whether the gravitational field in outer space can be determined without the knowledge of the density structure of the Earth but with the knowledge of the potential or other gravity field functions on the boundary.

A prior knowledge for the BVP is that the general determination of the gravitational field in space comes from the measurement on the boundary and the spatial behavior, described as a partial differential equation (PDE). The PDE for the interior BVP is the Poisson equation and for the exterior BVP is the Laplace equation (Sneeuw, 2006). In outer space the gravitational potential satisfies the Laplace equation:

$$\Delta V = 0 \tag{3.9}$$

where V is the gravitational potential and Δ is the Laplace operator. The divergence of the gravitational potential is zero which makes it a conservative field outside the boundary.

In terms of solving the BVP, the solution of the Laplace equation is the most important step. The Laplace equation can be solved both in Cartesian and spherical coordinates.

For the solution in Cartesian coordinates in outer space, the task is to solve:

$$\Delta V(x, y, z) = 0, \forall z > 0 \tag{3.10}$$

The solution of this equation is formulated by a series of base functions. For the horizontal domain (x and y coordinates), the base functions are Fourier series expressed with sines and cosines. For the vertical domain (z coordinate), the base functions are radial base functions. See detailed formula in Heiskanen and Moritz (1967).

The Laplace equation in spherical coordinates reads:

$$\Delta V = \frac{\partial^2 V}{\partial r^2} + \frac{2}{r}\frac{\partial^2 V}{\partial r} + \frac{1}{r^2}\frac{\partial^2 V}{\partial \theta^2} + \frac{\cot\theta}{r^2}\frac{\partial^2 V}{\partial \theta} + \frac{1}{r^2 \sin^2\theta}\frac{\partial^2 V}{\partial \lambda^2} = 0 \tag{3.11}$$

The solutions in spherical coordinates are harmonic functions. The base functions are the so called surface spherical harmonics:

$$Y_{lm}(\theta, \lambda) = P_{lm}(\cos\theta) \begin{cases} \cos m\lambda \\ \sin m\lambda \end{cases} \tag{3.12}$$

l and m are degree and order which are similar to the wave numbers in the Fourier series. The degree is always bigger or equal to the order.

The gravitational potential derived as a spherical harmonic function finally reads:

$$V(r, \theta, \lambda) = \frac{GM}{R} \sum_{l=0}^{\infty} (\frac{R}{r})^{l+1} \sum_{m=0}^{l} \bar{P}_{lm}(\cos\theta)(\bar{C}_{lm} \cos m\lambda + \bar{S}_{lm} \sin m\lambda) \tag{3.13}$$

where

r, θ, λ	spherical coordinates of the evaluated points
GM	geocentric constant
R	radius of the Earth
$\bar{P}_{lm}$	fully normalized associated Legendre functions
$\bar{C}_{lm}, \bar{S}_{lm}$	normalized dimensionless spherical harmonic coefficients

3.3 Legendre function

The Legendre functions and the base functions are orthogonal, but not orthonormal. It is necessary to normalize the Legendre functions and the base functions.

The normalization factor N_{lm}:

$$N_{lm} = \sqrt{(2-\delta_{m,0})(2l+1)\frac{(l-m)!}{(l+m)!}} \tag{3.14}$$

The normalized Legendre functions and the normalized base functions become:

$$\begin{aligned} \bar{Y}_{lm}(\theta,\lambda) &= N_{lm}Y_{lm}(\theta,\lambda) \\ \bar{P}_{lm}(\theta,\lambda) &= N_{lm}P_{lm}(\cos\theta) \end{aligned} \tag{3.15}$$

The numerical values of the normalized Legendre functions are required for the computation of the gravitational potentials and the gravity gradients. The strategy is to do the calculations recursively.

In figure 3.4, the calculation starts from the diagonal elements. The off-diagonal elements are calculated from the previous two horizontal elements with the same order recursively.

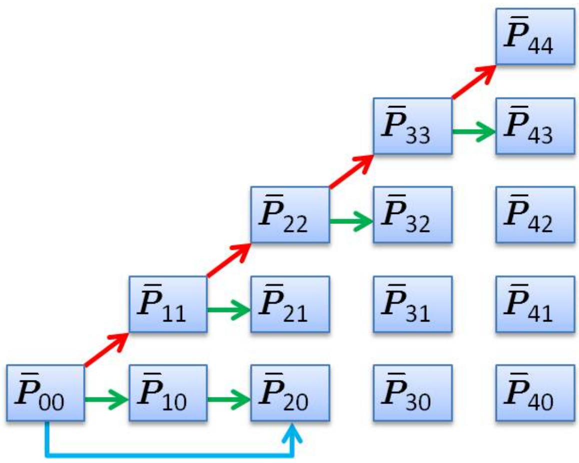

Figure 3.4: *Recursive calculation of Legendre functions*

The recursive relations (Heiskanen and Moritz, 1967) are

$$\begin{aligned} \bar{P}_{00}(\cos\theta) &= 1 \\ \bar{P}_{mm}(\cos\theta) &= W_{mm}(\sin\theta)\bar{P}_{m-1,m-1}(\cos\theta) \\ \bar{P}_{lm}(\cos\theta) &= W_{lm}[\cos\theta\bar{P}_{l-1,m}(\cos\theta) - W_{l-1,m}^{-1}\bar{P}_{l-2,m}(\cos\theta)] \end{aligned} \tag{3.16}$$

with

$$W_{11} = \sqrt{3}$$

$$W_{mm} = \sqrt{\frac{2m+1}{2m}} \tag{3.17}$$

$$W_{lm} = \sqrt{\frac{(2l+1)(2l-1)}{(l+m)(l-m)}}$$

Chapter 4

Gravity field recovery from low-low satellite-to-satellite tracking

4.1 Disturbing potential

The physical shape of the Earth is an irregular ellipsoid that can be approximated with a rotationally symmetric ellipsoid. The gravitational potential and the gravity field on this ellipsoid are called normal potential and normal gravity. The deviation between the real gravity potential W and the normal potential U is the disturbing potential T:

$$W = U + T \tag{4.1}$$

In the mathematical view, the normal field is the linear part when developing the real gravity field related observations into Taylor series with approximate values, which means:

$$\begin{aligned} U &= W_0 \\ T &= \delta W \end{aligned} \tag{4.2}$$

One of our purposes is to define the disturbing potential. Discussed in section 3.2, the quantities in equation 4.1 can be written in the form of spherical harmonic functions (Sneeuw, 2006):

$$W = \frac{GM}{r} + \frac{GM}{R} \sum_{l=2}^{\infty} \sum_{m=0}^{l} (\frac{R}{r})^{l+1} \bar{P}_{lm}(\cos\theta)(\bar{C}_{lm}\cos m\lambda + \bar{S}_{lm}\sin m\lambda) \tag{4.3a}$$

$$U = \frac{GM_0}{r} + \frac{GM_0}{R} \sum_{l=2}^{\infty} \sum_{m=0}^{l} (\frac{R}{r})^{l+1} \bar{P}_{lm}(\cos\theta)(\bar{c}_{lm}\cos m\lambda + \bar{s}_{lm}\sin m\lambda) \tag{4.3b}$$

$$T = \frac{\delta GM}{r} + \frac{GM_0}{R} \sum_{l=2}^{\infty} \sum_{m=0}^{l} (\frac{R}{r})^{l+1} \bar{P}_{lm}(\cos\theta)(\Delta\bar{C}_{lm}\cos m\lambda + \Delta\bar{S}_{lm}\sin m\lambda) \tag{4.3c}$$

For approximation GM_0 is used instead of GM which will lead to an error. However, this effect for $l \geq 2$ will be small.

The spherical harmonic coefficients of the disturbing potential are derived:

$$\begin{aligned}\Delta\bar{C}_{lm} &= \bar{C}_{lm} - \bar{c}_{lm} \\ \Delta\bar{S}_{lm} &= \bar{S}_{lm} - \bar{s}_{lm}\end{aligned} \tag{4.4}$$

Since the disturbing potential T can not be observed directly, the unknown quantities $\Delta\bar{C}_{lm}$ and $\Delta\bar{S}_{lm}$ have to be calculated from the real gravity field related observations. With the application of satellite geodesy techniques, it is possible to figure out a relation between the satellite observations and the unknowns.

4.2 Geometry of ll-SST

In the case of ll-SST (figure 4.1), two spacecraft are placed in the similar low polar orbits. One satellite is tracking another satellite with an inter-distance of up to a few hundreds of kilometers. The relative motion of the two spacecraft varies in space depending on the roughness of the gravity field features. The change of the relative motion is precisely measured by KBR system and the orbits are continuously tracked.

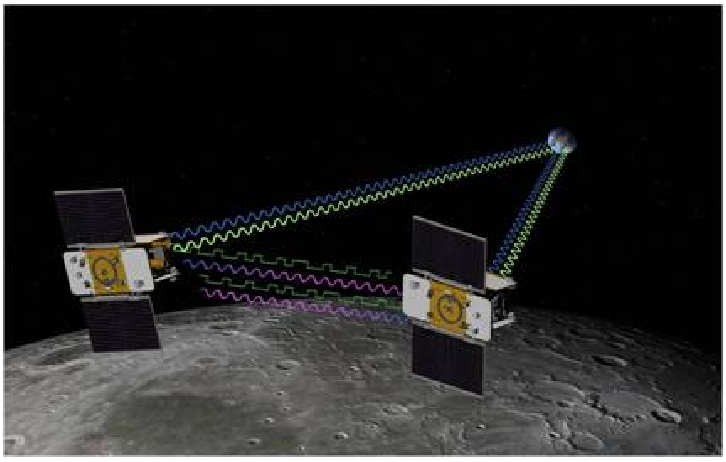

Figure 4.1: *Configuration of the twin satellites in ll-SST*

In order to establish the connection between the KBR measurements and the unknown quantities, it is necessary to understand the geometry of the twin satellites first (figure 4.2).

The inter-satellite range ρ is projected on the along track direction. The relative position $\mathbf{r}_{AB}$ is in the same direction as the base vector $\mathbf{e}_{AB}$.

The range can be calculated from the relative position and the base vector:

$$\rho = \|\mathbf{r}_A - \mathbf{r}_B\| = \mathbf{e}_{AB} \cdot \mathbf{r}_{AB} \tag{4.5}$$

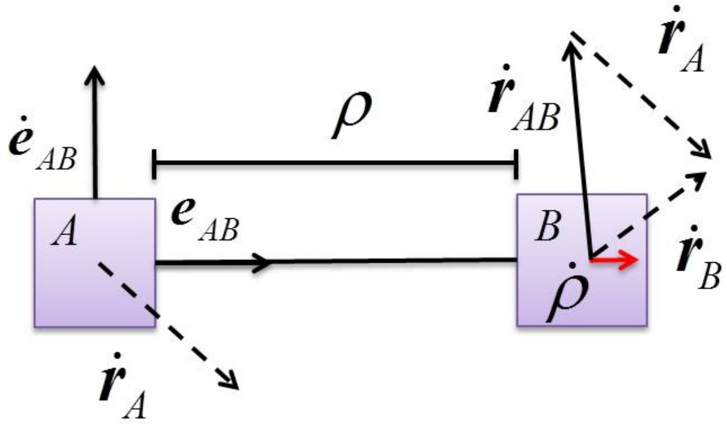

Figure 4.2: Geometry of ll-SST (Rummel et al. 1978)

The derivative of this equation leads to the range-rate. Since the cross track term is perpendicular to the along track term, the term $\dot{\mathbf{e}}_{AB} \cdot \mathbf{r}_{AB}$ equals zero, thus:

$$\dot{\rho} = \mathbf{e}_{AB} \cdot \dot{\mathbf{r}}_{AB} + \underbrace{\dot{\mathbf{e}}_{AB} \cdot \mathbf{r}_{AB}}_{0} = \mathbf{e}_{AB} \cdot \dot{\mathbf{r}}_{AB} \tag{4.6}$$

In a same way the range-acceleration is derived:

$$\ddot{\rho} = \mathbf{e}_{AB} \cdot \ddot{\mathbf{r}}_{AB} + \dot{\mathbf{e}}_{AB} \cdot \dot{\mathbf{r}}_{AB} \tag{4.7}$$

The term $\dot{\mathbf{e}}_{AB}$ can be calculated from:

$$\mathbf{r}_{AB} = \rho \cdot \mathbf{e}_{AB} \tag{4.8a}$$

$$\dot{\mathbf{r}}_{AB} = \dot{\rho} \cdot \mathbf{e}_{AB} + \rho \cdot \dot{\mathbf{e}}_{AB} \tag{4.8b}$$

$$\dot{\mathbf{e}}_{AB} = \frac{\dot{\mathbf{r}}_{AB} - \dot{\rho} \cdot \mathbf{e}_{AB}}{\rho} \tag{4.8c}$$

Inserting equation 4.8c into equation 4.7 yields:

$$\ddot{\rho} = \mathbf{e}_{AB} \cdot \ddot{\mathbf{r}}_{AB} + \frac{1}{\rho}(\dot{\mathbf{r}}_{AB}^2 - \dot{\rho}^2) \tag{4.9}$$

with

$$\begin{aligned} \ddot{\mathbf{r}}_{AB} &= 2\dot{\rho} \cdot \dot{\mathbf{e}}_{AB} + \ddot{\rho} \cdot \mathbf{e}_{AB} + \rho \cdot \ddot{\mathbf{e}}_{AB} \\ \ddot{\mathbf{e}}_{AB} &= \frac{\ddot{\mathbf{r}}_{AB} - 2\dot{\rho} \cdot \dot{\mathbf{e}}_{AB} - \ddot{\rho} \cdot \mathbf{e}_{AB}}{\rho} \end{aligned} \tag{4.10}$$

4.3 Gravity field modeling

Our target is to estimate the unknown spherical harmonic coefficients $\Delta\bar{C}_{lm}$ and $\Delta\bar{S}_{lm}$ of the disturbing potential from satellite observations. These observations include the GPS/DSN measurements and the KBR measurements. Most approaches are based on two physical laws: the energy conversation law and Newton's second law of motion.

4.3.1 Energy balance approach

The energy balance approach is based on the energy conservation law which states that the sum of the energy in a closed system is conserved. If only the conservative forces in a satellite system are considered, the sum of the kinetic energy E^{kin} and the potential E^{pot} is constant. The energy balance approach for the ll-SST model was refined by Jekeli (1999). The kinetic energy can be calculated from the satellite's velocity and the potential energy related to the gravitational field and the altitude of the satellite (Weigelt, 2007).

The kinetic energy difference between the two satellites is given as:

$$E^{kin}_{AB} = \frac{1}{2}(|\dot{\mathbf{x}}_B|^2 - |\dot{\mathbf{x}}_A|^2) = \frac{1}{2}(\dot{\mathbf{x}}_B - \dot{\mathbf{x}}_A)^T(\dot{\mathbf{x}}_B + \dot{\mathbf{x}}_A) \tag{4.11}$$

Inserting equation 4.8b into equation 4.11 leads to:

$$E^{kin}_{AB} = \frac{1}{2}[\dot{\rho}(\dot{\mathbf{x}}_B + \dot{\mathbf{x}}_A)^T\mathbf{e}_{AB} + \rho(\dot{\mathbf{x}}_B + \dot{\mathbf{x}}_A)^T\dot{\mathbf{e}}_{AB}] \tag{4.12}$$

which is the representation of the relative kinetic energy by KBR measurements.

4.3.2 Acceleration approach

The acceleration approach is based on Newton's equation of motion. It exploits the formula for the range-acceleration $\ddot{\rho}$ by analytical twofold numerical differentiation of the equation of the range ρ (equation 4.5) as (compare equation 4.9):

$$\ddot{\rho} - \frac{1}{\rho}(\dot{\mathbf{r}}^2_{AB} - \dot{\rho}^2) = \mathbf{e}_{AB} \cdot \ddot{\mathbf{r}}_{AB} \tag{4.13}$$

The satellite velocities $\dot{\mathbf{r}}^{A/B}$ can be determined from the orbits $\mathbf{r}^{A/B}$ by means of numerical differentiation. Two modifications of the acceleration approach exist: the pointwise acceleration approach (Austen and Grafarend, 2004; Novák et al., 2006) and the average acceleration approach (Liu, 2008). The pointwise acceleration approach makes use of polynomials of higher order (i.e. 9-point schemes, Reubelt et al. 2003, 2006) for numerical derivation of pointwise values for $\dot{\mathbf{r}}^{A/B}$ and $\ddot{\rho}$ while the average acceleration approach applies a simple 3-point scheme to generate average accelerations (Liu, 2008), which necessitates the application of an averaging filter to the functional model.

4.3.3 Short-arc approach

The mathematical model of the short-arc approach comes from Newton's equation of motion (Mayer-Gürr et al., 2005):

$$\ddot{\mathbf{r}}(t) = \mathbf{f}(t; \mathbf{r}, \dot{\mathbf{r}}; \mathbf{x}; \mathbf{b}) \tag{4.14}$$

where $\mathbf{r}$ are the satellite positions estimated from the GPS/DSN measurements at the epoch t , $\mathbf{f}$ is the force function acting on the satellite, $\mathbf{x}$ are the gravity field parameters (influences from tides are neglected) and $\mathbf{b}$ refer to the orbit related parameters (coordinates of the boundary points of every arc).

The solution of Newton's equation of motion, formulated as a boundary value problem according to Schneider (1968):

$$\mathbf{r}(\tau) = (1-\tau)\mathbf{r}_A + \tau\mathbf{r}_B + T^2 \int_0^1 K(\tau, \tau')\mathbf{f}(t; \mathbf{r}, \dot{\mathbf{r}}; \mathbf{x}; \mathbf{b}) d\tau' \tag{4.15}$$

with the boundary values

$$\begin{aligned} \mathbf{r}_A &= \mathbf{r}(t_A) \\ \mathbf{r}_B &= \mathbf{r}(t_B) \end{aligned} \tag{4.16}$$

In equation 4.15, T (do not confuse with the disturbing potential T) is the time interval of one single arc. The normalized time variable τ is denoted as:

$$\tau = \frac{t - t_A}{T}, \quad t \in [t_A, t_B], \quad T = t_B - t_A \tag{4.17}$$

The integral kernel K is given as:

$$K(\tau, \tau') = \begin{cases} \tau(1-\tau'), & \tau \leq \tau' \\ \tau'(1-\tau), & \tau' \leq \tau \end{cases} \tag{4.18}$$

where K can be regarded as the different weight of every single position.

The force function $\mathbf{f}$ in equation 4.14 can be developed into Taylor series:

$$\mathbf{f}(t; \mathbf{r}, \dot{\mathbf{r}}; \mathbf{x}; \mathbf{b}) = \mathbf{f}_S(t; \mathbf{r}, \dot{\mathbf{r}}; \mathbf{b}^0) + \mathbf{f}_{\Delta S}(t; \mathbf{r}, \dot{\mathbf{r}}; \Delta\mathbf{b}) + \mathbf{f}_E(t; \mathbf{r}, \dot{\mathbf{r}}; \mathbf{x}^0) + \mathbf{f}_{\Delta E}(t; \mathbf{r}, \dot{\mathbf{r}}; \Delta\mathbf{x}) \tag{4.19}$$

where

$\mathbf{f}_S(t; \mathbf{r}, \dot{\mathbf{r}}; \mathbf{b}^0)$	reference orbit-related parameters
$\mathbf{f}_{\Delta S}(t; \mathbf{r}, \dot{\mathbf{r}}; \Delta\mathbf{b})$	unknown corrections to the orbit-related parameters
$\mathbf{f}_E(t; \mathbf{r}, \dot{\mathbf{r}}; \mathbf{x}^0)$	reference gravity field parameters
$\mathbf{f}_{\Delta E}(t; \mathbf{r}, \dot{\mathbf{r}}; \Delta\mathbf{x})$	unknown corrections to the gravity field parameters

Inserting equation 4.19 into equation 4.15 yields:

$$\begin{aligned}\mathbf{r}(\tau) = (1-\tau)\mathbf{r}_A + \tau\mathbf{r}_B + T^2\int_0^1 K(\tau,\tau')\mathbf{f}_S(t;\mathbf{r},\dot{\mathbf{r}};\mathbf{b}^0)d\tau' \\ + T^2\int_0^1 K(\tau,\tau')\mathbf{f}_{\Delta S}(t;\mathbf{r},\dot{\mathbf{r}};\Delta\mathbf{b})d\tau' \\ + T^2\int_0^1 K(\tau,\tau')\mathbf{f}_E(t;\mathbf{r},\dot{\mathbf{r}};\mathbf{x}^0)d\tau' \\ + T^2\int_0^1 K(\tau,\tau')\mathbf{f}_{\Delta E}(t;\mathbf{r},\dot{\mathbf{r}};\Delta\mathbf{x})d\tau'\end{aligned} \tag{4.20}$$

With the reference values $\mathbf{x}_0$, $\mathbf{b}_0$ and the estimated parameters $\Delta\mathbf{x}$, $\Delta\mathbf{b}$, the evaluated parameters for the real gravity field are achieved:

$$\begin{aligned}\hat{\mathbf{x}} &= \mathbf{x}_0 + \Delta\mathbf{x} \\ \hat{\mathbf{b}} &= \mathbf{b}_0 + \Delta\mathbf{b}\end{aligned} \tag{4.21}$$

The term $\mathbf{f}_{\Delta E}(t;\mathbf{r},\dot{\mathbf{r}};\Delta\mathbf{x})$ is identical with the disturbing potential T in equation 4.1. In equation 4.20, the relation between the observations and the unknown gravity field parameters are finally defined.

4.4 Mathematical model of the short-arc approach

The short-arc approach has been successfully applied to derive the ITG-CHAMP01, ITG-CHAMP02 (Mayer-Gürr et al., 2005) and ITG-GRACE series of gravity field models (Mayer-Gürr, 2006). The equations presented in this section are mainly from Mayer-Gürr (2006). The data processing strategy and the modifications based on this method are demonstrated. For more details please refer to Mayer-Gürr (2006).

4.4.1 Setup of the mathematical model

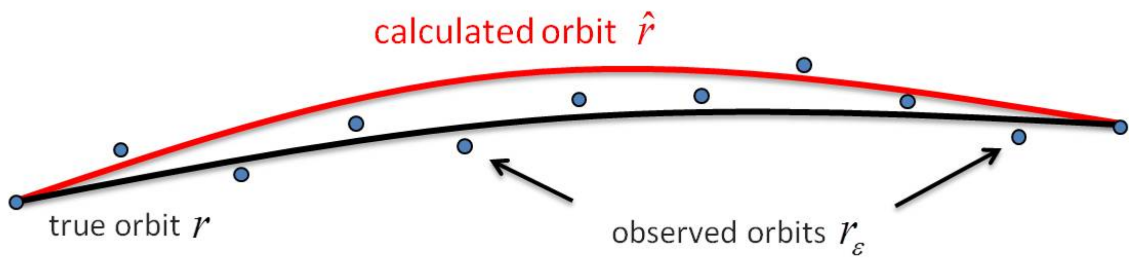

Figure 4.3: *Configuration of one short arc*

Figure 4.3 shows the configuration of one short arc. The green dots $\mathbf{r}_\varepsilon$ are GPS/DSN observations of the satellite positions which contain noise. The black arc represents the error free positions of the satellite. The black arc, as mentioned in equation 4.15, can be formulated as:

$$\mathbf{r}(\tau) = (1-\tau)\mathbf{r}_A + \tau\mathbf{r}_B + T^2 \int_0^1 K(\tau,\tau')\mathbf{f}(\mathbf{r}(\tau')d\tau' \tag{4.22}$$

Inserting $\mathbf{r}_\varepsilon$ into equation 4.22 leads to $\hat{\mathbf{r}}$:

$$\hat{\mathbf{r}}(\tau) = (1-\tau)\mathbf{r}_A + \tau\mathbf{r}_B + T^2 \int_0^1 K(\tau,\tau')\mathbf{f}(\mathbf{r}_\varepsilon(\tau')d\tau' \tag{4.23}$$

where $\hat{\mathbf{r}}$ is the calculated path derived from the boundary value equation that should be distinguished from the error free path $\mathbf{r}$.

The subtraction between equation 4.23 and equation 4.22 yields:

$$\mathbf{r}(\tau) - \hat{\mathbf{r}}(\tau) = T^2 \int_0^1 K(\tau,\tau')[\mathbf{f}(\mathbf{r}(\tau')) - \mathbf{f}(\mathbf{r}_\varepsilon(\tau'))]d\tau' \tag{4.24}$$

with the integral operator

$$\kappa = T^2 \int_0^1 K(\tau,\tau')(\cdot)d\tau' \tag{4.25}$$

In a simplified case is

$$\mathbf{r} - \hat{\mathbf{r}} = \kappa[\mathbf{f}(\mathbf{r}) - \mathbf{f}(\mathbf{r}_\varepsilon)] \tag{4.26}$$

with Taylor Expansion

$$\mathbf{f}(\mathbf{r}) = \mathbf{f}(\mathbf{r}_\varepsilon) + \nabla\mathbf{f}|_{\mathbf{r}_\varepsilon} \cdot (\mathbf{r} - \hat{\mathbf{r}}) + \ldots \tag{4.27}$$

where $\mathbf{r}_\varepsilon$ are assumed as the approximate positions to develop the Taylor series.

So equation 4.26 becomes:

$$\mathbf{r} - \hat{\mathbf{r}} = \kappa\nabla\mathbf{f}(\mathbf{r} - \mathbf{r}_\varepsilon) \tag{4.28}$$

Replace $\hat{\mathbf{r}}$ with equation 4.23:

$$[\mathbf{I} - \kappa\nabla\mathbf{f}(\mathbf{r}_\varepsilon)](\mathbf{r} - \mathbf{r}_\varepsilon) = \kappa\mathbf{f}(\mathbf{r}_\varepsilon) + \mathbf{b} - \mathbf{r}_\varepsilon \tag{4.29}$$

where $\mathbf{I}$ is the unit matrix.

Equation 4.29 can be rewritten as:

$$\Delta\mathbf{r} = \mathbf{r} - \mathbf{r}_\varepsilon = [\mathbf{I} - \kappa\nabla\mathbf{f}(\mathbf{r}_\varepsilon)]^{-1}[\kappa\mathbf{f}(\mathbf{r}_\varepsilon) + \mathbf{b} - \mathbf{r}_\varepsilon] \tag{4.30}$$

Equation 4.30 can be discretized in terms of orbit observations:

$$\Delta\mathbf{r} = (\mathbf{I} - \mathbf{KT})^{-1}(\mathbf{Kf} + \mathbf{Bb} - \mathbf{r}_\varepsilon) \tag{4.31}$$

where $\mathbf{K}$ is the matrix of the numerical integration and $\mathbf{B}$ is the design matrix of the boundary values. The reference positions are derived from the measured positions.

The gravity gradient (for calculation refer to Appendix A and Baur 2007) is denoted as:

$$\mathbf{T} = \begin{pmatrix} \nabla \mathbf{f}(\tau_1) & & 0 \\ & \ddots & \\ 0 & & \nabla \mathbf{f}(\tau_N) \end{pmatrix} \tag{4.32}$$

$\Delta \mathbf{r}$ in equation 4.31 are the coordinate differences between the noisy positions $\mathbf{r}_\varepsilon$ and the error free positions $\mathbf{r}$. The reference positions along the trajectory of the twin satellites from the measured positions are

$$\mathbf{r}_0^{A/B} = \mathbf{r}_\varepsilon^{A/B} + \Delta \mathbf{r}^{A/B} \tag{4.33}$$

with

$$\Delta \mathbf{r}^{A/B} = (\mathbf{I} - \mathbf{K}\mathbf{T}^{A/B})^{-1}(\mathbf{K}\mathbf{f}_0^{A/B} + \mathbf{B}\mathbf{b}_0^{A/B} - \mathbf{r}_\varepsilon^{A/B}) \tag{4.34}$$

where $\mathbf{f}_0$ and $\mathbf{b}_0$ are calculated with $\mathbf{r}_\varepsilon$ other than $\mathbf{r}$.

Linearization:

The linearization includes two parts: for the orbit (satellite positions) and for the KBR measurements.

For the orbit:

Equation 4.33 and equation 4.34 define the relation between the orbit and the unknown quantities.

The partial derivatives for the unknowns from the relative positions are

$$\begin{aligned} \mathbf{R}^{A/B} &= \frac{\partial \mathbf{r}^{A/B}}{\partial \mathbf{f}} = (\mathbf{I} - \mathbf{K}\mathbf{T}^{A/B})^{-1}\mathbf{K} \\ \bar{\mathbf{B}}^{A/B} &= \frac{\partial \mathbf{r}^{A/B}}{\partial \mathbf{b}} = (\mathbf{I} - \mathbf{K}\mathbf{T}^{A/B})^{-1}\mathbf{B} \end{aligned} \tag{4.35}$$

The relative acceleration can be calculated from the relative position:

$$\ddot{\mathbf{r}}_0^{A/B} = \mathbf{f}_0^{A/B} + \mathbf{T}^{A/B}\Delta \mathbf{r}^{A/B} \tag{4.36}$$

The partial derivatives for the unknowns from the relative acceleration are

$$\begin{aligned} \ddot{\mathbf{R}}^{A/B} &= \frac{\partial \ddot{\mathbf{r}}^{A/B}}{\partial \mathbf{f}} = \mathbf{I} + \mathbf{T}^{A/B}\mathbf{R}^{A/B} \\ \ddot{\mathbf{B}}^{A/B} &= \frac{\partial \ddot{\mathbf{r}}^{A/B}}{\partial \mathbf{b}} = \mathbf{T}^{A/B}\mathbf{R}^{A/B} \end{aligned} \tag{4.37}$$

The relative velocity can be calculated from the relative acceleration:

$$\dot{\mathbf{r}}_0^{A/B} = \dot{\mathbf{K}}\ddot{\mathbf{r}}_0^{A/B} + \dot{\mathbf{B}}\mathbf{b}_0^{A/B} \tag{4.38}$$

The partial derivatives for the unknowns from the relative velocity are

$$\begin{aligned} \dot{\mathbf{R}}^{A/B} &= \frac{\partial \dot{\mathbf{r}}^{A/B}}{\partial \mathbf{f}} = \dot{\mathbf{K}}\ddot{\mathbf{R}}^{A/B} \\ \dot{\mathbf{B}}^{A/B} &= \frac{\partial \dot{\mathbf{r}}^{A/B}}{\partial \mathbf{b}} = \dot{\mathbf{B}} + \dot{\mathbf{K}}\ddot{\mathbf{B}}^{A/B} \end{aligned} \tag{4.39}$$

For the KBR measurments:

Similar to equation 4.14, the connection between the KBR measurements and the unknown quantities can be defined:

$$\begin{aligned} \rho(t) &= \mathbf{f}(t; \mathbf{r}_{AB}; \mathbf{x}; \mathbf{b}_A, \mathbf{b}_B) \\ \dot{\rho}(t) &= \mathbf{f}(t; \mathbf{r}_{AB}, \dot{\mathbf{r}}_{AB}; \mathbf{x}; \mathbf{b}_A, \mathbf{b}_B) \\ \ddot{\rho}(t) &= \mathbf{f}(t; \mathbf{r}_{AB}, \dot{\mathbf{r}}_{AB}, \ddot{\mathbf{r}}_{AB}; \mathbf{x}; \mathbf{b}_A, \mathbf{b}_B) \end{aligned} \tag{4.40}$$

The partial derivatives of the observation equations 4.40 w.r.t the searched for gravity field parameters yields:

$$\begin{aligned} \frac{\partial \rho}{\partial \mathbf{x}} &= \frac{\partial \rho}{\partial \mathbf{r}_{AB}}\left(\frac{\partial \mathbf{r}_B}{\partial \mathbf{x}} - \frac{\partial \mathbf{r}_A}{\partial \mathbf{x}}\right) \\ \frac{\partial \dot{\rho}}{\partial \mathbf{x}} &= \frac{\partial \dot{\rho}}{\partial \mathbf{r}_{AB}}\left(\frac{\partial \mathbf{r}_B}{\partial \mathbf{x}} - \frac{\partial \mathbf{r}_A}{\partial \mathbf{x}}\right) + \frac{\partial \dot{\rho}}{\partial \dot{\mathbf{r}}_{AB}}\left(\frac{\partial \dot{\mathbf{r}}_B}{\partial \mathbf{x}} - \frac{\partial \dot{\mathbf{r}}_A}{\partial \mathbf{x}}\right) \\ \frac{\partial \ddot{\rho}}{\partial \mathbf{x}} &= \frac{\partial \ddot{\rho}}{\partial \mathbf{r}_{AB}}\left(\frac{\partial \mathbf{r}_B}{\partial \mathbf{x}} - \frac{\partial \mathbf{r}_A}{\partial \mathbf{x}}\right) + \frac{\partial \ddot{\rho}}{\partial \dot{\mathbf{r}}_{AB}}\left(\frac{\partial \dot{\mathbf{r}}_B}{\partial \mathbf{x}} - \frac{\partial \dot{\mathbf{r}}_A}{\partial \mathbf{x}}\right) + \frac{\partial \ddot{\rho}}{\partial \ddot{\mathbf{r}}_{AB}}\left(\frac{\partial \ddot{\mathbf{r}}_B}{\partial \mathbf{x}} - \frac{\partial \ddot{\mathbf{r}}_A}{\partial \mathbf{x}}\right) \end{aligned} \tag{4.41}$$

and the same holds for the arc-related parameters:

$$\begin{aligned} \frac{\partial \rho}{\partial \mathbf{b}} &= \frac{\partial \rho}{\partial \mathbf{r}_{AB}}\left(\frac{\partial \mathbf{r}_B}{\partial \mathbf{b}} - \frac{\partial \mathbf{r}_A}{\partial \mathbf{b}}\right) \\ \frac{\partial \dot{\rho}}{\partial \mathbf{b}} &= \frac{\partial \dot{\rho}}{\partial \mathbf{r}_{AB}}\left(\frac{\partial \mathbf{r}_B}{\partial \mathbf{b}} - \frac{\partial \mathbf{r}_A}{\partial \mathbf{b}}\right) + \frac{\partial \dot{\rho}}{\partial \dot{\mathbf{r}}_{AB}}\left(\frac{\partial \dot{\mathbf{r}}_B}{\partial \mathbf{b}} - \frac{\partial \dot{\mathbf{r}}_A}{\partial \mathbf{b}}\right) \\ \frac{\partial \ddot{\rho}}{\partial \mathbf{b}} &= \frac{\partial \ddot{\rho}}{\partial \mathbf{r}_{AB}}\left(\frac{\partial \mathbf{r}_B}{\partial \mathbf{b}} - \frac{\partial \mathbf{r}_A}{\partial \mathbf{b}}\right) + \frac{\partial \ddot{\rho}}{\partial \dot{\mathbf{r}}_{AB}}\left(\frac{\partial \dot{\mathbf{r}}_B}{\partial \mathbf{b}} - \frac{\partial \dot{\mathbf{r}}_A}{\partial \mathbf{b}}\right) + \frac{\partial \ddot{\rho}}{\partial \ddot{\mathbf{r}}_{AB}}\left(\frac{\partial \ddot{\mathbf{r}}_B}{\partial \mathbf{b}} - \frac{\partial \ddot{\mathbf{r}}_A}{\partial \mathbf{b}}\right) \end{aligned} \tag{4.42}$$

with the partial differentials

$$\begin{aligned} &\frac{\partial \rho}{\partial \mathbf{r}_{AB}} = \mathbf{e}_{AB} \\ &\frac{\partial \dot{\rho}}{\partial \mathbf{r}_{AB}} = \dot{\mathbf{e}}_{AB}, \frac{\partial \dot{\rho}}{\partial \dot{\mathbf{r}}_{AB}} = \mathbf{e}_{AB}, \\ &\frac{\partial \ddot{\rho}}{\partial \mathbf{r}_{AB}} = \ddot{\mathbf{e}}_{AB}, \frac{\partial \ddot{\rho}}{\partial \dot{\mathbf{r}}_{AB}} = 2\dot{\mathbf{e}}_{AB}, \frac{\partial \ddot{\rho}}{\partial \ddot{\mathbf{r}}_{AB}} = \mathbf{e}_{AB}, \end{aligned} \tag{4.43}$$

Design matrix:

For the orbit, the design matrix for the gravity field parameters is $\frac{\partial \mathbf{r}}{\partial \mathbf{x}}$ and for the arc-related parameters is $\frac{\partial \mathbf{r}}{\partial \mathbf{b}}$. It will be called one-step linearization in this thesis.

For the KBR measurements, the design matrix is the multiplication of two partial differentials $\frac{\partial \mathbf{l}}{\partial \mathbf{r}_{AB}} \cdot \frac{\partial \mathbf{r}_{AB}}{\partial \mathbf{x}}$ for the gravity field parameters and $\frac{\partial \mathbf{l}}{\partial \mathbf{r}_{AB}} \cdot \frac{\partial \mathbf{r}_{AB}}{\partial \mathbf{b}}$ for the arc-related parameters. It will be called two-step linearization in this thesis.

The first part $\frac{\partial \mathbf{l}}{\partial \mathbf{r}_{AB}}$ of the two-step linearization is denoted as matrix $\mathbf{P}$:

$$\mathbf{P} = \begin{pmatrix} \frac{\partial \rho}{\partial \mathbf{r}_{AB}} & 0 & 0 \\ \frac{\partial \dot{\rho}}{\partial \mathbf{r}_{AB}} & \frac{\partial \dot{\rho}}{\partial \dot{\mathbf{r}}_{AB}} & 0 \\ \frac{\partial \ddot{\rho}}{\partial \mathbf{r}_{AB}} & \frac{\partial \ddot{\rho}}{\partial \dot{\mathbf{r}}_{AB}} & \frac{\partial \ddot{\rho}}{\partial \ddot{\mathbf{r}}_{AB}} \end{pmatrix} \tag{4.44}$$

The elements in matrix $\mathbf{P}$ refer to equation 4.43 and section 4.2.

Approximate values:

In section 4.2 the geometry of the twin satellites is defined. Based on this geometry, the approximate range ρ_0, range-rate $\dot{\rho}_0$ and range-acceleration $\ddot{\rho}_0$ can be calculated from the approximate positions $\mathbf{r}_0^A$ and $\mathbf{r}_0^B$.

The relative position, velocity and acceleration are

$$\begin{aligned} \mathbf{r}_0^{AB} &= \mathbf{r}_0^B - \mathbf{r}_0^A \\ \dot{\mathbf{r}}_0^{AB} &= \dot{\mathbf{r}}_0^B - \dot{\mathbf{r}}_0^A \\ \ddot{\mathbf{r}}_0^{AB} &= \ddot{\mathbf{r}}_0^B - \ddot{\mathbf{r}}_0^A \end{aligned} \tag{4.45}$$

with the base vector

$$\mathbf{e}^{A/B}(t_i) = \frac{\mathbf{r}_0^B(t_i) - \mathbf{r}_0^A(t_i)}{\|\mathbf{r}_0^B(t_i) - \mathbf{r}_0^A(t_i)\|} \tag{4.46}$$

The approximate range, range-rate and range acceleration are

$$\begin{aligned} \rho_0(t_i) &= \mathbf{e}_0^{A/B}(t_i) \cdot \mathbf{r}_0^{A/B}(t_i) \\ \dot{\rho}_0(t_i) &= \mathbf{e}_0^{A/B}(t_i) \cdot \dot{\mathbf{r}}_0^{A/B}(t_i) \\ \ddot{\rho}_0(t_i) &= \mathbf{e}_0^{A/B}(t_i) \cdot \ddot{\mathbf{r}}_0^{A/B}(t_i) + \frac{1}{\rho_0(t_i)}(\dot{\mathbf{r}}_0^{A/B}(t_i)^2 - \dot{\rho}_0(t_i)^2) \end{aligned} \tag{4.47}$$

Observation equation:

Finally the observation equations for the orbit and the KBR measurements are obtained.

For the orbit:

$$\mathbf{r}_\varepsilon^{A/B} - \mathbf{r}_0^{A/B} = \underbrace{\mathbf{R}^{A/B}\mathbf{G}^{A/B}}_{\frac{\partial \mathbf{r}}{\partial \mathbf{f}} \cdot \frac{\partial \mathbf{f}}{\partial \mathbf{x}}} \Delta \mathbf{x} + \underbrace{\bar{\mathbf{B}}^{A/B}}_{\frac{\partial \mathbf{r}}{\partial \mathbf{b}}} \Delta \mathbf{b}^{A/B} \tag{4.48}$$

and for the KBR measurements:

$$\mathbf{l} = \begin{pmatrix} \rho - \rho_0 \\ \dot{\rho} - \dot{\rho}_0 \\ \ddot{\rho} - \ddot{\rho}_0 \end{pmatrix} = \mathbf{P} \underbrace{\begin{pmatrix} \mathbf{R}^B & -\mathbf{R}^A \\ \dot{\mathbf{R}}^B & -\dot{\mathbf{R}}^A \\ \ddot{\mathbf{R}}^B & -\ddot{\mathbf{R}}^A \end{pmatrix} \begin{pmatrix} \mathbf{G}^B \\ \mathbf{G}^A \end{pmatrix}}_{\frac{\partial \mathbf{l}}{\partial \mathbf{r}_{AB}} \cdot \frac{\partial \mathbf{r}_{AB}}{\partial \mathbf{f}} \cdot \frac{\partial \mathbf{f}}{\partial \mathbf{x}}} \Delta\mathbf{x} + \mathbf{P} \underbrace{\begin{pmatrix} \bar{\mathbf{B}}^B & -\bar{\mathbf{B}}^A \\ \dot{\bar{\mathbf{B}}}^B & -\dot{\bar{\mathbf{B}}}^A \\ \ddot{\bar{\mathbf{B}}}^B & -\ddot{\bar{\mathbf{B}}}^A \end{pmatrix}}_{\frac{\partial \mathbf{l}}{\partial \mathbf{r}_{AB}} \cdot \frac{\partial \mathbf{r}_{AB}}{\partial \mathbf{b}}} \begin{pmatrix} \Delta\mathbf{b}^B \\ \Delta\mathbf{b}^A \end{pmatrix} \tag{4.49}$$

This is the final linearized model for the observations with necessary approximations. Equation 4.48 is the exact observation equation for high-low SST of the short-arc method. Since the KBR measurements have to be positioned with the information of the orbit, equation 4.49 is applied together with equation 4.48 for ll-SST analysis.

Finally the estimated gravity field and arc-related parameters are achieved:

$$\begin{aligned} \hat{\mathbf{x}} &= \mathbf{x}_0 + \Delta\mathbf{x} \\ \hat{\mathbf{b}} &= \mathbf{b}_0 + \Delta\mathbf{b} \end{aligned} \tag{4.50}$$

For the arrangement of all matrices mentioned in this section for programming, please refer to Appendix A and B.

4.4.2 Modification of the short-arc method

Several modifications for deriving the final observation equation have been made for the application in this thesis. Both Mayer-Gürr's method and the modified method have been tested. In this section the modified observation equation is presented.

Equation 4.48 is the observation equation for the orbit that has one-step linearization.

$$\mathbf{r}_{\varepsilon}^{A/B} - \mathbf{r}_0^{A/B} = \mathbf{R}^{A/B}\mathbf{G}^{A/B}\Delta\mathbf{x} + \bar{\mathbf{B}}^{A/B}\Delta\mathbf{b}^{A/B} \tag{4.51}$$

Rearrange it for the two satellites separately:

$$\mathbf{r}_{\varepsilon}^{A} - \mathbf{r}_0^{A} = \mathbf{R}^{A}\mathbf{G}^{A}\Delta\mathbf{x} + \bar{\mathbf{B}}^{A}\Delta\mathbf{b}^{A} \tag{4.52a}$$

$$\mathbf{r}_{\varepsilon}^{B} - \mathbf{r}_0^{B} = \mathbf{R}^{B}\mathbf{G}^{B}\Delta\mathbf{x} + \bar{\mathbf{B}}^{B}\Delta\mathbf{b}^{B} \tag{4.52b}$$

Equation 4.52a minus equation 4.52b leads to:

$$\mathbf{r}_{\varepsilon}^{AB} - \mathbf{r}_0^{AB} = (\mathbf{R}^{B}\mathbf{G}^{B} - \mathbf{R}^{A}\mathbf{G}^{A})\Delta\mathbf{x} + \begin{pmatrix} \bar{\mathbf{B}}^{B}, -\bar{\mathbf{B}}^{A} \end{pmatrix} \begin{pmatrix} \Delta\mathbf{b}^B \\ \Delta\mathbf{b}^A \end{pmatrix} \tag{4.53}$$

Equation 4.53 multiplied by $\mathbf{e}_0^{AB}$ yields:

$$\mathbf{e}_0^{AB} \cdot \mathbf{r}_{\varepsilon}^{AB} - \rho_0^{AB} = \mathbf{e}_0^{AB} \cdot (\mathbf{R}^{B}\mathbf{G}^{B} - \mathbf{R}^{A}\mathbf{G}^{A})\Delta\mathbf{x} + \mathbf{e}_0^{AB} \begin{pmatrix} \bar{\mathbf{B}}^{B}, -\bar{\mathbf{B}}^{A} \end{pmatrix} \begin{pmatrix} \Delta\mathbf{b}^B \\ \Delta\mathbf{b}^A \end{pmatrix} \tag{4.54}$$

The range observation equation in equation 4.49 is

$$\rho_\varepsilon^{AB} - \rho_0^{AB} = \mathbf{P}(\mathbf{R}^B\mathbf{G}^B - \mathbf{R}^A\mathbf{G}^A)\Delta\mathbf{x} + \mathbf{P}\begin{pmatrix} \bar{\mathbf{B}}^B, -\bar{\mathbf{B}}^A \end{pmatrix}\begin{pmatrix} \Delta\mathbf{b}^B \\ \Delta\mathbf{b}^A \end{pmatrix} \tag{4.55}$$

Equation 4.55 is very similar to equation 4.54.

In Mayer-Gürr's method, the design matrix $\mathbf{P}$ is derived from Taylor expansion through equation 4.41 and 4.42 which means $\mathbf{P} = \mathbf{e}_0^{AB}$ for the range observation equation here.

Then equation 4.55 becomes:

$$\rho_\varepsilon^{AB} - \rho_0^{AB} = \mathbf{e}_0^{AB}(\mathbf{R}^B\mathbf{G}^B - \mathbf{R}^A\mathbf{G}^A)\Delta\mathbf{x} + \mathbf{e}_0^{AB}\begin{pmatrix} \bar{\mathbf{B}}^B, -\bar{\mathbf{B}}^A \end{pmatrix}\begin{pmatrix} \Delta\mathbf{b}^B \\ \Delta\mathbf{b}^A \end{pmatrix} \tag{4.56}$$

Now compare equation 4.56 with equation 4.54. There is a difference between the term ρ_ε^{AB} and the term $\mathbf{e}_0^{AB} \cdot \mathbf{r}_\varepsilon^{AB}$. The inconsistency between these two terms will lead to different results calculated from equation 4.56 and equation 4.54.

To estimate this difference, the modified observation equation derives the new design matrix $\mathbf{P}'$ not from two-step linearization but from equation 4.53 directly.

In this case $\mathbf{P}' = \mathbf{e}_\varepsilon^{AB}$ holds for the range observation equation. Equation 4.53 multiplied by $\mathbf{P}'$ yields:

$$\mathbf{e}_\varepsilon^{AB} \cdot \mathbf{r}_\varepsilon^{AB} - \mathbf{e}_\varepsilon^{AB} \cdot \mathbf{r}_0^{AB} = \mathbf{e}_\varepsilon^{AB} \cdot (\mathbf{R}^B\mathbf{G}^B - \mathbf{R}^A\mathbf{G}^A)\Delta\mathbf{x} + \mathbf{e}_\varepsilon^{AB}\begin{pmatrix} \bar{\mathbf{B}}^B, -\bar{\mathbf{B}}^A \end{pmatrix}\begin{pmatrix} \Delta\mathbf{b}^B \\ \Delta\mathbf{b}^A \end{pmatrix} \tag{4.57}$$

With the term $\rho_0'^{AB} = \mathbf{e}_\varepsilon^{AB} \cdot \mathbf{r}_0^{AB}$, the modified range observation equation becomes:

$$\rho_\varepsilon^{AB} - \rho_0'^{AB} = \mathbf{P}'(\mathbf{R}^B\mathbf{G}^B - \mathbf{R}^A\mathbf{G}^A)\Delta\mathbf{x} + \mathbf{P}'\begin{pmatrix} \bar{\mathbf{B}}^B, -\bar{\mathbf{B}}^A \end{pmatrix}\begin{pmatrix} \Delta\mathbf{b}^B \\ \Delta\mathbf{b}^A \end{pmatrix} \tag{4.58}$$

The same work for the range-rate and range-acceleration observation equations leads to the new $\mathbf{P}'$ matrix:

$$\mathbf{P}' = \begin{pmatrix} \mathbf{e}_\varepsilon^{AB} & 0 & 0 \\ 0 & \mathbf{e}_\varepsilon^{AB} & 0 \\ 0 & \frac{1}{\rho_\varepsilon}(\dot{\mathbf{r}}_\varepsilon^{AB} - \dot{\rho}_\varepsilon^{AB}\mathbf{e}_\varepsilon^{AB}) & \mathbf{e}_\varepsilon^{AB} \end{pmatrix} \tag{4.59}$$

The final modified observation equation is achieved:

$$\begin{pmatrix} \rho - \rho_0' \\ \dot{\rho} - \dot{\rho}_0' \\ \ddot{\rho} - \ddot{\rho}_0' \end{pmatrix} = \mathbf{P}'\begin{pmatrix} \mathbf{R}^B & -\mathbf{R}^A \\ \dot{\mathbf{R}}^B & -\dot{\mathbf{R}}^A \\ \ddot{\mathbf{R}}^B & -\ddot{\mathbf{R}}^A \end{pmatrix}\begin{pmatrix} \mathbf{G}^B \\ \mathbf{G}^A \end{pmatrix}\Delta\mathbf{x} + \mathbf{P}'\begin{pmatrix} \bar{\mathbf{B}}^B & -\bar{\mathbf{B}}^A \\ \dot{\bar{\mathbf{B}}}^B & -\dot{\bar{\mathbf{B}}}^A \\ \ddot{\bar{\mathbf{B}}}^B & -\ddot{\bar{\mathbf{B}}}^A \end{pmatrix}\begin{pmatrix} \Delta\mathbf{b}^B \\ \Delta\mathbf{b}^A \end{pmatrix} \tag{4.60}$$

with

$$\begin{pmatrix} \rho - \rho_0' \\ \dot{\rho} - \dot{\rho}_0' \\ \ddot{\rho} - \ddot{\rho}_0' \end{pmatrix} = \mathbf{P}'\begin{pmatrix} \mathbf{r}_\varepsilon - \mathbf{r}_0 \\ \dot{\mathbf{r}}_\varepsilon - \dot{\mathbf{r}}_0 \\ \ddot{\mathbf{r}}_\varepsilon - \ddot{\mathbf{r}}_0 \end{pmatrix} \tag{4.61}$$

Both Mayer-Guerr's original observation equation and the modified observation equation have been tested. The two different **P** matrices only lead to a very small difference around magnitude of 10^{-17} in the output Degree Root Mean Square (DE-RMS) signals which overlap with each other in figure 4.4. Compared with the reference signal, this magnitude of difference can be ignored. So the two observation equations will not be distinguished in the thesis. However, the modified $\mathbf{P}'$ is simpler than the original **P** matrix and it is easier to arrange the elements.

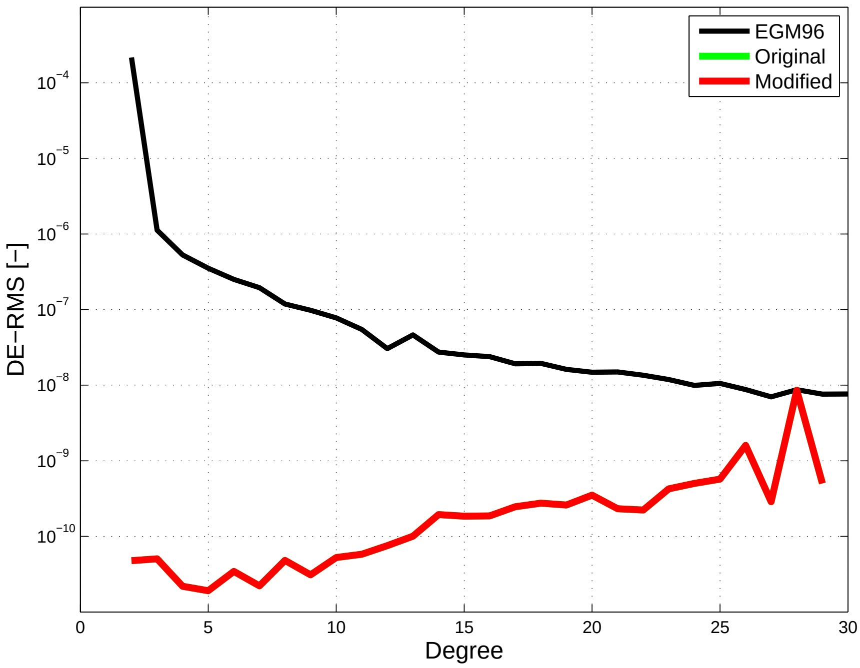

Figure 4.4: DE-RMS of the results from applying the original and modified equations. Simulation scenario: Input Orbit: EGM96 (degree 30); Reference field: Eigen-grace02s (degree 29)

4.4.3 Elimination of parameters

In the observation equation 4.49, the unknown quantities include the gravity field parameters $\mathbf{x}$ (spherical harmonic coefficients) and the arc-related parameters $\mathbf{b}$ (boundary positions of every single arc).

For every short arc, there are six unknowns of the boundary values for one satellite. In terms of one month continuous observations with an interval of 5 seconds, there are around 2,500 arcs (200 points per single arc). Those arc-related unknowns already lead to a very large number of parameters, even much more than the gravity field coefficients (e.g. 8277 unknown spherical harmonic coefficients up to degree 90). Considering the memory of the computer and the run time, it is difficult to calculate all unknown parameters.

The best solution is to reduce the size of the normal equations. The unknowns of the boundary values can be eliminated before the arcs merge into the complete system of the normal equations.

To apply least-squares adjustment, equation 4.49 can be rewritten as:

$$\mathbf{l} = \mathbf{A}\mathbf{x} + \mathbf{B}\mathbf{y} + \mathbf{e} \tag{4.62}$$

where $\mathbf{l}$ is the observation vector, $\mathbf{A}$ and $\mathbf{B}$ are the design matrices, $\mathbf{x}$ and $\mathbf{y}$ are the unknowns, $\mathbf{e}$ is the vector of residuals.

Rearrange equation 4.62:

$$\mathbf{l} = \begin{pmatrix} \mathbf{A} & \mathbf{B} \end{pmatrix} \begin{pmatrix} \mathbf{x} \\ \mathbf{y} \end{pmatrix} + \mathbf{e} \tag{4.63}$$

The normal equation for one short arc is

$$\begin{pmatrix} \mathbf{A}^T\mathbf{A} & \mathbf{A}^T\mathbf{B} \\ \mathbf{B}^T\mathbf{A} & \mathbf{B}^T\mathbf{B} \end{pmatrix} \begin{pmatrix} \hat{\mathbf{x}} \\ \hat{\mathbf{y}} \end{pmatrix} = \begin{pmatrix} \mathbf{A}^T\mathbf{l} \\ \mathbf{B}^T\mathbf{l} \end{pmatrix} \tag{4.64}$$

The vector $\hat{\mathbf{x}}$ can be estimated without solving the whole system.

Rewrite equation 4.64 as:

$$\begin{aligned} \mathbf{A}^T\mathbf{A}\hat{\mathbf{x}} + \mathbf{A}^T\mathbf{B}\hat{\mathbf{y}} &= \mathbf{A}^T\mathbf{l} \\ \mathbf{B}^T\mathbf{A}\hat{\mathbf{x}} + \mathbf{B}^T\mathbf{B}\hat{\mathbf{y}} &= \mathbf{B}^T\mathbf{l} \end{aligned} \tag{4.65}$$

To solve equation 4.65, we first get:

$$\hat{\mathbf{y}} = (\mathbf{B}^T\mathbf{B})^{-1}\mathbf{B}^T\mathbf{l} - (\mathbf{B}^T\mathbf{B})^{-1}\mathbf{B}^T\mathbf{A}\hat{\mathbf{x}} \tag{4.66}$$

Substitute equation 4.66 for $\hat{\mathbf{y}}$ in equation 4.65:

$$(\mathbf{A}^T\mathbf{A} - \mathbf{A}^T\mathbf{B}(\mathbf{B}^T\mathbf{B})^{-1}\mathbf{B}^T\mathbf{A})\hat{\mathbf{x}} = \mathbf{A}^T\mathbf{l} - \mathbf{A}^T\mathbf{B}(\mathbf{B}^T\mathbf{B})^{-1}\mathbf{B}^T\mathbf{l} \tag{4.67}$$

The normal equations are

$$\begin{aligned} &\mathbf{N}_{11} = \mathbf{A}^T\mathbf{A} \quad \mathbf{N}_{12} = \mathbf{A}^T\mathbf{B} \quad \mathbf{N}_{22} = \mathbf{B}^T\mathbf{B} \\ &n_1 = \mathbf{A}^T\mathbf{l} \quad n_2 = \mathbf{B}^T\mathbf{l} \end{aligned} \tag{4.68}$$

Since the tracking data of the satellite orbits and the KBR measurements have different accuracies, it is necessary to set up a weight matrix:

$$\mathbf{P} = \begin{pmatrix} p_1 & & & \\ & p_2 & & \\ & & \ddots & \\ & & & p_i \end{pmatrix} \tag{4.69}$$

where p_i represents the weight for the ith point in one arc.

The normal equations then become:

$$\begin{aligned} \mathbf{N}_{11} &= \mathbf{A}^T\mathbf{P}\mathbf{A} \quad \mathbf{N}_{12} = \mathbf{A}^T\mathbf{P}\mathbf{B} \quad \mathbf{N}_{22} = \mathbf{B}^T\mathbf{P}\mathbf{B} \\ n_1 &= \mathbf{A}^T\mathbf{P}\mathbf{l} \quad n_2 = \mathbf{B}^T\mathbf{P}\mathbf{l} \end{aligned} \tag{4.70}$$

Finally the unknowns $\hat{\mathbf{x}}$ are derived:

$$\begin{aligned} \bar{\mathbf{N}} &= \mathbf{N}_{11} - \mathbf{N}_{12}\mathbf{N}_{22}^{-1}\mathbf{N}_{12}^T \\ \bar{n} &= n_1 - \mathbf{N}_{12}\mathbf{N}_{22}^{-1}n_2 \\ \hat{\mathbf{x}} &= \bar{\mathbf{N}}^{-1}\bar{n} \end{aligned} \tag{4.71}$$

Chapter 5

Results

The GRAIL mission has accomplished its prime science phase and is in the extended science phase (section 2.2.3). However, it is not possible to process the real data (not available yet) without much additional work (e.g processing exact frame rotations and disturbing forces). Hence all the analyses provided in this chapter are based on the simulated orbits and simulated KBR measurements (one month period).

The program has been applied on simulated GRACE data first and then moved to simulated GRAIL data. The purpose of the simulation study, including inversion of the gravity field parameters and quality assessment, is to make the preparation for the real data application.

The code is programmed in Matlab and has been tested for more than one thousand times under different simulation scenarios. Since the short-arc approach requires a high computational effort, the run time of the program for the high degree case (i.e. degree 90) is up to 10 hours with an 8 GByte Random Access Memory (RAM) computer. In order to save time, many tests have been undertaken in the low degree case (i.e. degree 30).

5.1 Setting parameters

Our aim is to estimate the gravity field parameters from the simulated data. The input parameters of the program include not only the reference gravity field, but also different variable settings. Two key variable settings discussed here are the arc length and the weight matrix.

Two quantities are defined to evaluate the quality of the solutions. The first one is the DE-RMS denoted as:

$$DE-RMS_l = \sqrt{\frac{1}{N}\sum_{m=0}^{l} \Delta v_{lm}^2} \tag{5.1}$$

which reflects the noise of every degree.

Another one are the relative empirical errors (REE) (noise to signal ratio):

$$e^{rel}_{vlm} = \left\| \frac{\Delta v_{lm}}{v^{ref}_{lm}} \right\| \tag{5.2}$$

with

$$\begin{aligned} v_{lm} &= \begin{cases} \bar{C}_{lm} & m \geq 0 \\ \bar{S}_{lm} & m < 0 \end{cases} \\ \Delta v_{lm} &= v^{ref}_{lm} - \hat{v}_{lm} \end{aligned} \tag{5.3}$$

where Δv_{lm} is the noise of every coefficient, v^{ref}_{lm} is the input coefficient.

The length of the short arc is a natural choice (Mayer-Gürr et al., 2005): if the arc length is too short, it will lead to a huge number of the arc-related unknowns and may also disturb the longer wavelengths; if it is too long, accumulated effects will arise.

From the previous experience, the best possible choice of the arc length is between 1/3 and 1/2 of the satellite revolution, but it really depends on how the scenario is set up. Mayer-Gürr used 30 minutes for GRACE (sampling rate: 5 seconds) whereas tests from this thesis show that 21 minutes (260 points per arc) for GRACE and 9 minutes (100 points per arc) for GRAIL are good choices.

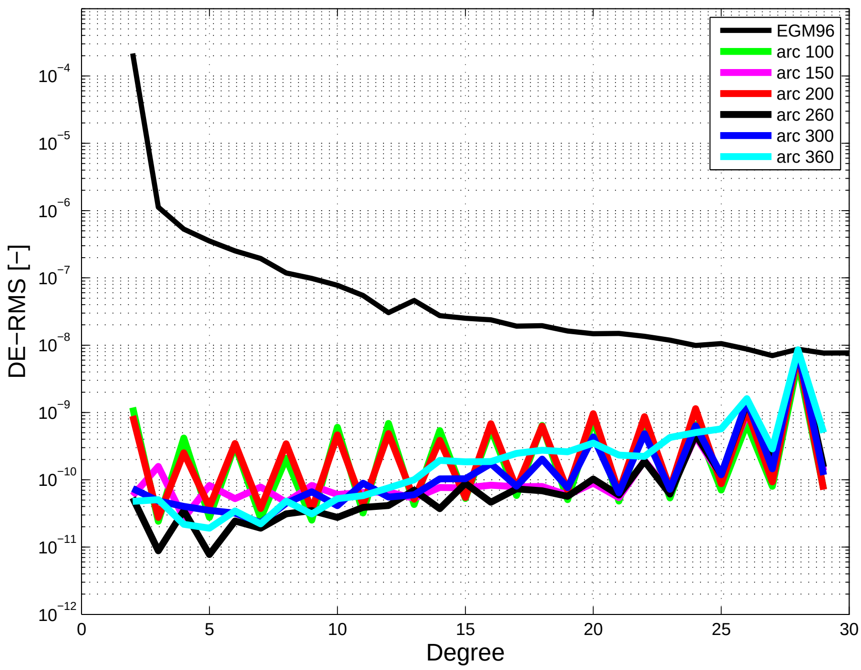

Figure 5.1: *DE-RMS of results from testing with different arc lengths. Simulation scenario: Input Orbit: EGM96 (degree 30); Reference field: Eigen-grace02s (degree 29)*

For a convenient expression of the arc length, we assume that *arc* 100 means there are 100 points per arc with a sampling rate of 5 seconds.

Figure 5.1 is an example to display the effect of the different arc lengths. The arc 260 achieves the smallest DE-RMS and is the best choice. Through this kind of tests can we find out the best arc length for GRACE or GRAIL simulation scenarios. An important remark is that once the best arc length is found, it can be fixed for all solutions in the GRACE or GRAIL simulation scenarios.

However, the setting of the weight matrix varies for every particular scenario. For every scenario, different weight factors are necessary to be tested.

Similarly, for a convenient expression, we assume *weight* 100 means that the position of the satellite has a weight of one and the KBR measurement has a weight of 100. For documentary the best choices of the weight factors have been recorded. The arc-wise weight matrix is not considered in this thesis. For the arc-wise weight matrix arrangement it is referred to Mayer-Gürr (2006).

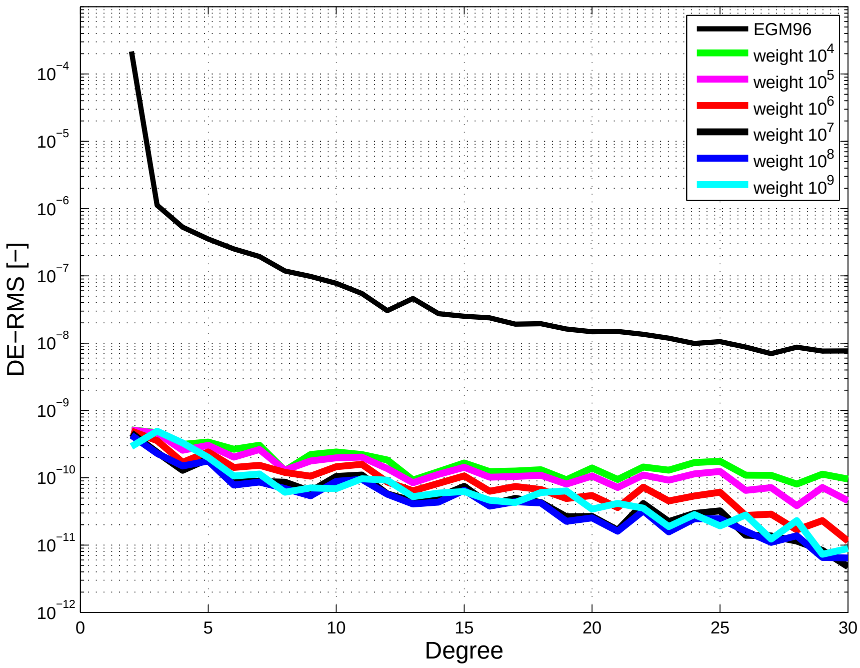

Figure 5.2: *DE-RMS of results from testing with different weight factors. Simulation scenario: Input Orbit: EGM96 (degree 30); Reference field: Eigen-grace02s (degree 30)*

In figure 5.2, the dark blue curve yields the best result. Even so, since every test has one magnitude difference, the best result achieved so far still has a space for improvement with better choices of the weight factor.

5.2 GRACE simulation study

Orbit simulation:

The GRACE orbit is simulated with the following parameters (Table 5.1):

Table 5.1: *Orbit simulation parameters*

Parameter	Quantity
Geocentric constant	$GM = 3.986004418 \cdot 10^{14}\ \mathrm{m}^3\mathrm{s}^{-2}$
Radius	$R = 6378136.6$ m
Inclination	$i = 89°$
Sampling rate	$\Delta t = 5$ s
Separation	Around 200 km
Altitude	Around 500 km
Period	1 month
Gravity field model	EGM96

5.2.1 Simulation scenario: noise free

In this simulation scenario, all simulated observations are noise free.

(1) 90-90 noise free simulation scenario

In the 90-90 noise free simulation scenario, the orbit and the KBR measurements are simulated with the gravity field model EGM96 (Lemoine et al., 1998) up to degree 90. The reference gravity field model is Eigen-grace02s (Reigber et al., 2005) up to degree 90 as well. It is a "perfect" simulation scenario since there is no inconsistency contributed by noise or coefficients' deficiency (spectral aliasing). Therefore, it is not necessary to set up the weight matrix.

Figure 5.3 demonstrates the differences (DE-RMS) between the estimated gravity field models and the input gravity field model. The estimated gravity field models are calculated from the simulated range (green), range-rate (red) and range-acceleration (blue) measurements separately.

In the mid-degrees, the three DE-RMS signals overlap with each other at the magnitude of 10^{-14}. The comparably large error at the beginning can be explained from the fact that GRACE is not sensitive to the coefficient C_{20} because of the design (Ries et al., 2008).

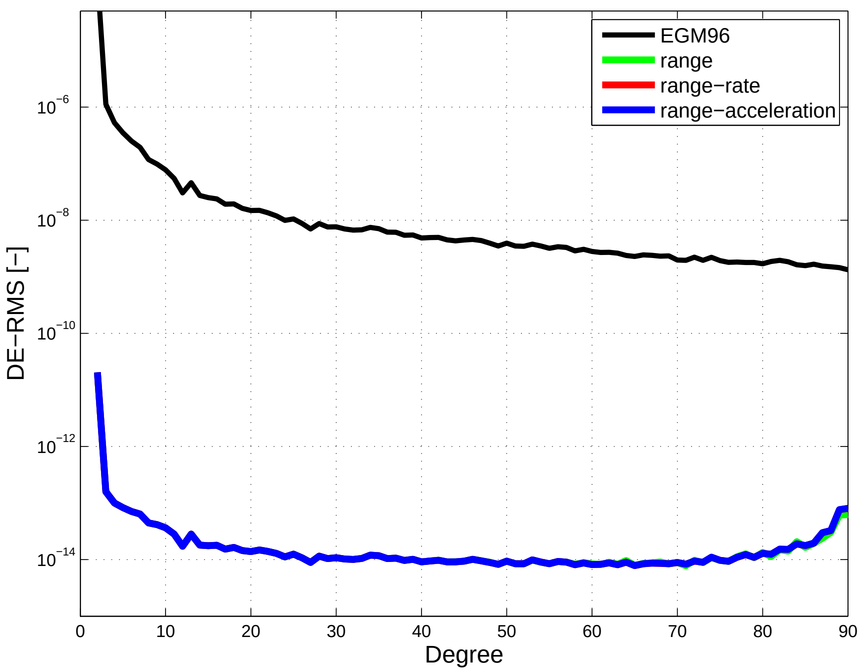

Figure 5.3: *DE-RMS of GRACE 90-90 simulation: noise free*

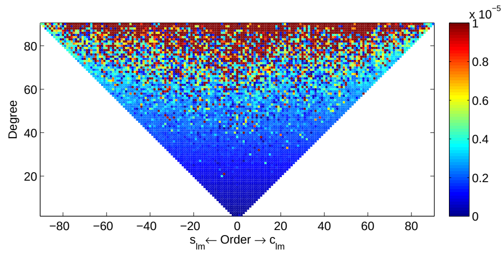

(a) Range

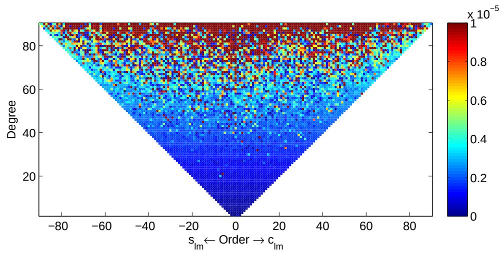

(b) Range-rate

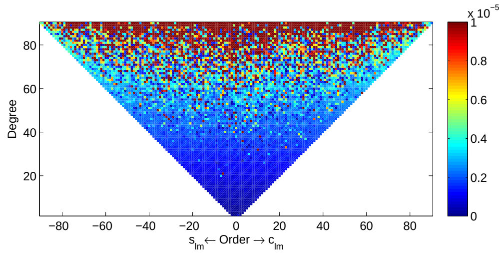

(c) Range-acceleration

Figure 5.4: *REE of GRACE 90-90 simulation: noise free*

The REE in figure 5.4 interpret the noise of every single coefficient. Compared with the input signal itself, the noise to signal ratios are rather small (around 10^{-5}). Under such conditions, it can be concluded that the output gravity field models equal the input gravity field model. It also means the program is basically working, but for quality assessment more tests are necessary.

(2) 90-80 noise free simulation scenario

In this simulation scenario, the orbit and the KBR measurements are still simulated with the gravity field model EGM96 up to degree 90. But the reference gravity field model Eigen-grace02s is varied to degree 80. The output field is then up to degree 80. This simulation scenario will have the inconsistency from the coefficients' deficiency.

The neglect of 10 degree coefficients in the reference gravity field exaggerates the inconsistency. The DE-RMS are getting closer to the reference signal (figure 5.5) and the REE are increasing (figure 5.6) as the degree grows. The overall performances of the range (green) and range-rate (red) resolutions are almost at the same magnitude, but the performance of the range-acceleration (blue) resolution is about a half magnitude worse.

There are two possible reasons for it: by differentiation (from range-rates to range accelerations) the signal on higher degrees is amplified. This means that the unmodeled signal between degree 80 and 90 becomes stronger and leads to larger spectral aliasing. Another reason is that for this scenario a weight matrix is necessary (it is not a perfect scenario because of the coefficient's deficiency), but the choices for the factors in the weight matrix (table 5.2) are coming from the empirical experience. Through this way, one can never tell the best factors have been chosen. Thus it is possible to have an improved resolution with better choices of the factors.

Table 5.2: *Documentary of weight factors*

Observation	Factor
Range	10^4
Range-rate	10^7
Range-acceleration	10^9

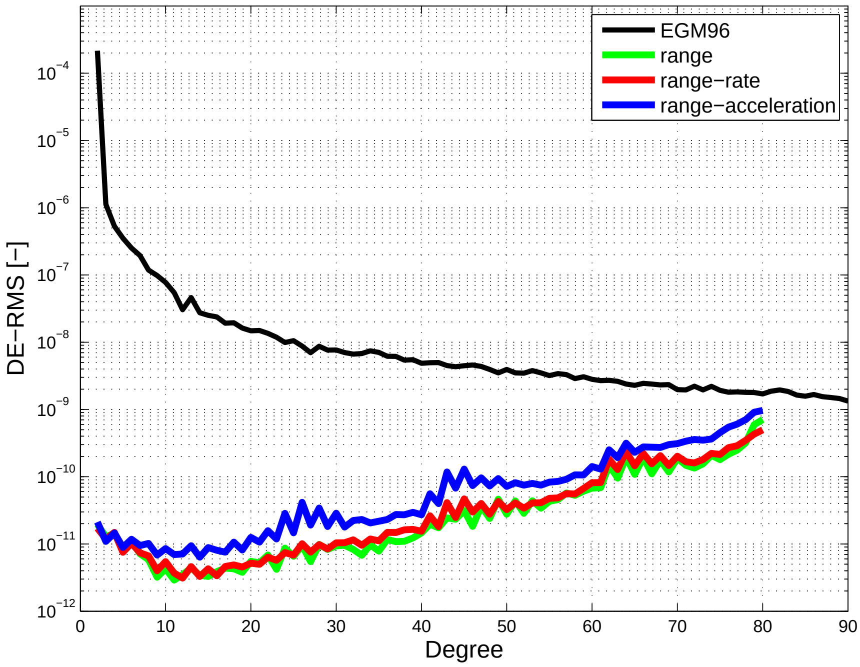

Figure 5.5: *DE-RMS of GRACE 90-80 simulation: noise free*

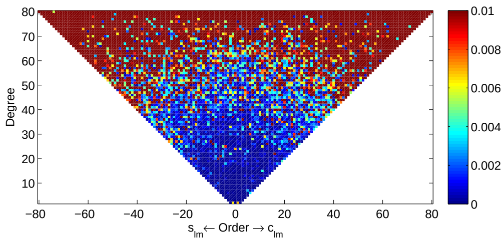

(a) Range

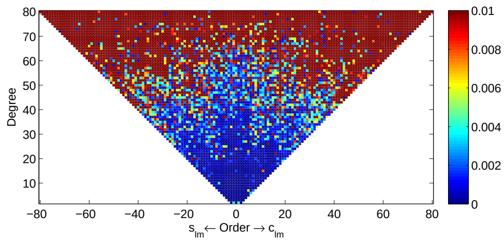

(b) Range-rate

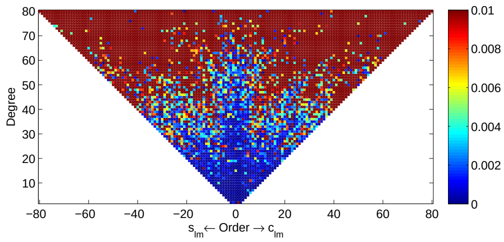

(c) Range-acceleration

Figure 5.6: *REE of GRACE 90-80 simulation: noise free*

5.2.2 Simulation scenario: with white noise

White noise simulation:

The standard deviations of the white noises are listed in table 5.3. For the orbits, the white noises are added to the measurements in every direction.

Table 5.3: *Simulated white noise*

Observation	White noise
Orbit	3 cm
Range	1 μm
Range-rate	1 $\mu m/s$
Range-acceleration	1 μGal

(1) 90-90 simulation scenario: with white noise

This simulation scenario will have the inconsistency contributed by the white noise.

The overall trends of the the three DE-RMS outputs in figure 5.7 and the REE in figure 5.8 are similar to those in the 90-80 noise free simulation scenario. However, the noises introduced to these three KBR measurements are not comparable and the noise of range-accelerations is too pessimistic compared to the others. Therefore, to guarantee a fair comparison, the best option is to introduce the noise for ranges and generate the noises for range-rates and range-accelerations by means of differentiation or error propagation.

The choices for the factors in the weight matrix are listed in table 5.4.

Table 5.4: *Documentary of weight factors*

Observation	Factor
Range	10^6
Range-rate	10^{10}
Range-acceleration	10^{11}

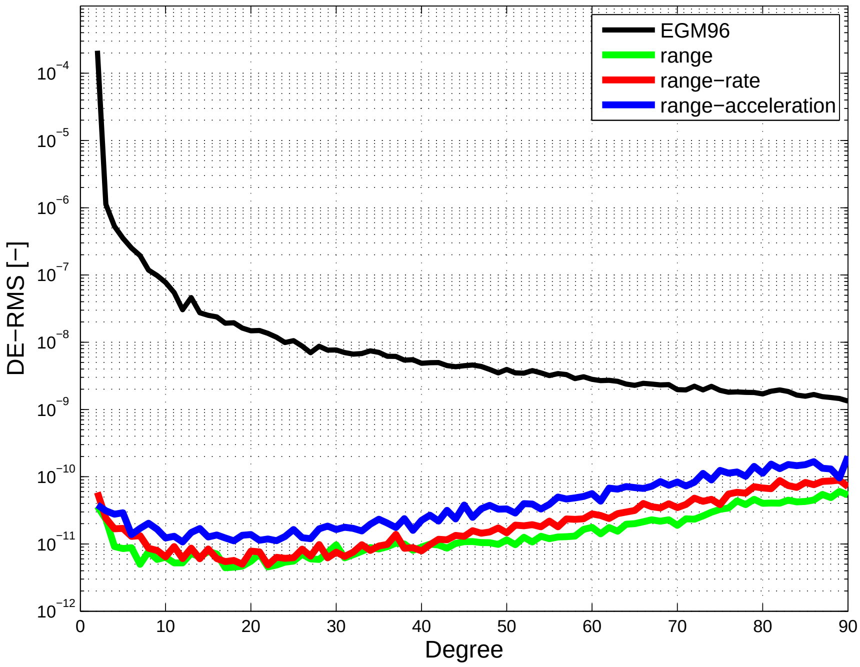

Figure 5.7: *DE-RMS of GRACE 90-90 simulation: with white noise*

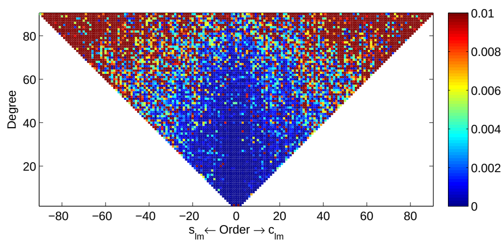

(a) Range

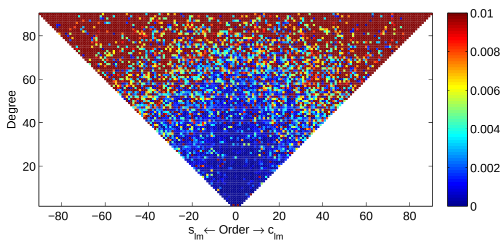

(b) Range-rate

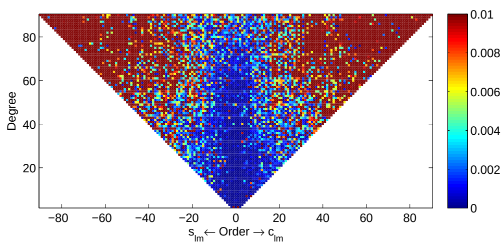

(c) Range-acceleration

Figure 5.8: *REE of GRACE 90-90 simulation: with white noise*

(2) 90-80 simulation scenario: with white noise

This simulation scenario is a more realistic scenario since the real gravity field parameters have infinite degrees and the real data have stochastic noises.

The three resolutions are impacted by the inconsistencies from the white noise and the coefficients'deficiency. The overall magnitudes of the DE-RMS signals (figure 5.9) and the REE (figure 5.10) are the largest among the previous simulation scenarios. However, according to the results of a similar simulation scenario provided by Mayer-Gürr et al. (2004), the DE-RMS with a overall magnitude of 10^{-11} in mid-degrees is quite reasonable.

The weight matrix factors are listed (table 5.5):

Table 5.5: *Documentary of weight factors*

Observation	Factor
Range	10^5
Range-rate	10^8
Range-acceleration	10^{10}

One important remark is that from the tests it also shows more iterations will not lead to an obvious improvement. Thus all the resolutions presented in the simulation scenarios are only calculated in one iteration.

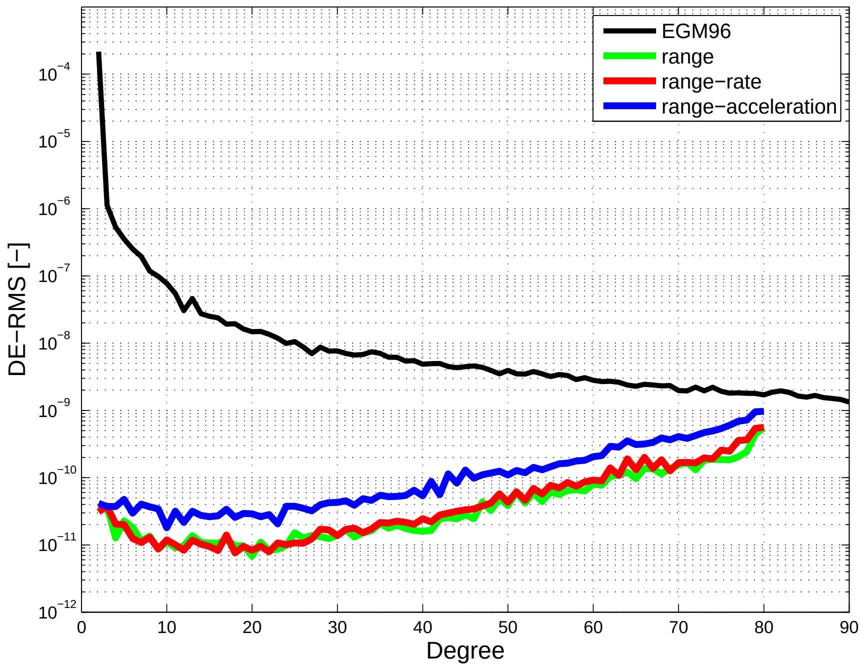

Figure 5.9: *DE-RMS of GRACE 90-80 simulation: with white noise*

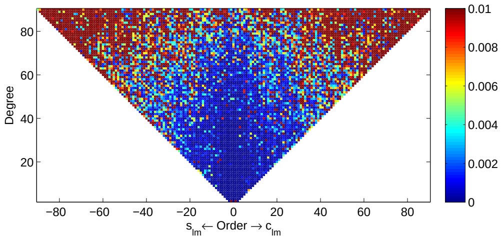

(a) Range

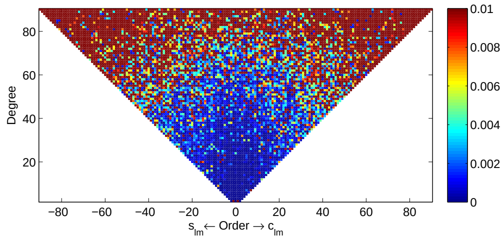

(b) Range-rate

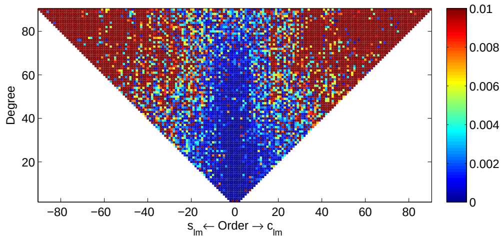

(c) Range-acceleration

Figure 5.10: *REE of GRACE 90-80 simulation: with white noise*

5.3 GRAIL simulation study

The GRACE simulation study has provided promising results and the next step is to move it to GRAIL. Experience on GRACE indicates that the resolutions suffer the inconsistencies from the stochastic noises and the coefficients'deficiency.

However, the problem of the coefficients'deficiency can not be overcome in the realistic case because the real gravity field model is regarded as having infinite degrees. Thus, the quality assessment for GRAIL will mainly focus on the effect of the stochastic noises (i.e. white noise).

In chapter 1 the LRO mission was introduced which was designed to provide a detailed survey of the Moon. The knowledge of the position accuracy has been defined: 50-100 m in total position and 1 m radially (Vondrak et al., 2010; Mazarico et al., 2012). With the addition of altimetric crossovers and radiometric-only orbits, the total position accuracy (RMS) could be around 12 m (Mazarico et al., 2012). Additionally, the position accuracy in the radial direction is much better than that in the along-track and cross-track directions.

The simulation scenarios are divided into the orbit fixed simulation and the range fixed simulation.

Orbit simulation:

The GRAIL orbit is simulated with the following parameters (Table 5.6):

Table 5.6: *Orbit simulation parameters*

Parameter	Quantity
Gravitational constant	$GM = 4.902800000 \cdot 10^{14}$ m^{3}s^{-2}
Radius	$R = 1738000$ m
Inclination	$i = 89°$
Sampling rate	$\Delta t = 5$ s
Separation	Around 90 km
Altitude	Around 50 km
Period	1 month
Gravity field model	JGL160P1

(1) 160-80 range fixed simulation scenario

In this simulation scenario, the orbit is simulated with the gravity field model JGL160P1 (Chin et al., 2007) up to degree 160. The reference gravity field model is JGL150Q1 (Chin et al., 2007) up to degree 80.

Fixed white noises are added to the range measurements whereas different levels of white noises are added to the orbits (table 5.7).

Table 5.7: Simulated white noise

Observation	White noise
Orbit 1	3 cm
Orbit 2	50 cm
Orbit 3	1 m
Orbit 4	10 m
Orbit 5	100 m
Range	1 μm

In figure 5.11, the output signals are obviously affected by the increasing orbit noises. When the orbit accuracy is up to 100 m, the maximum resolution is only around degree 50 where the DE-RMS signal intersects with the reference signal.

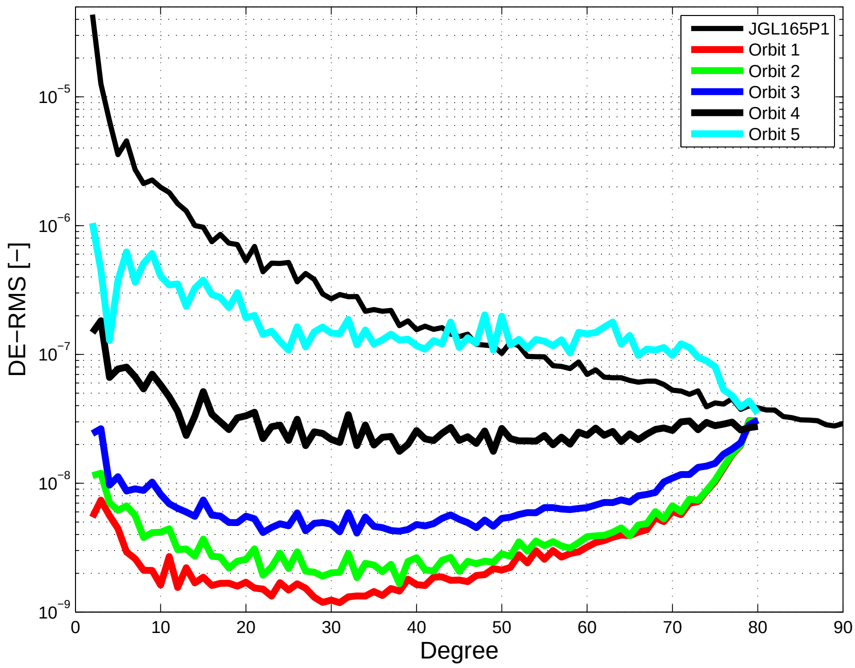

Figure 5.11: DE-RMS of GRAIL 160-80 range fixed simulation

The REE in figure 5.12 show that the different orbit accuracies have tremendous influences on the sectorial and tesseral coefficients, but almost no impacts on the zonal coefficients. This phenomenon can be explained from the flights of the twin satellites: the twin satellites fly behind each other in polar orbits which will lead to the best coverage of the zonal area as the moon rotates and results in a North-South striping pattern.

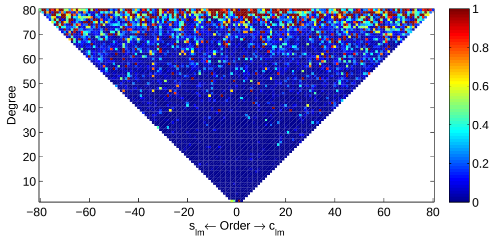

(a) Orbit 1

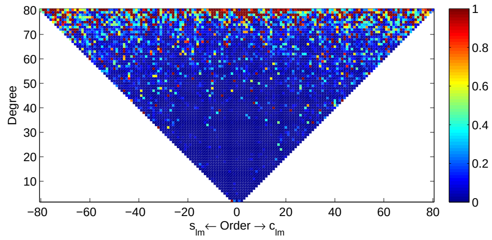

(b) Orbit 2

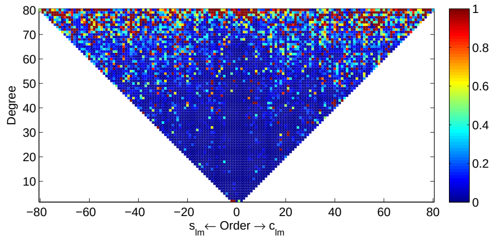

(c) Orbit 3

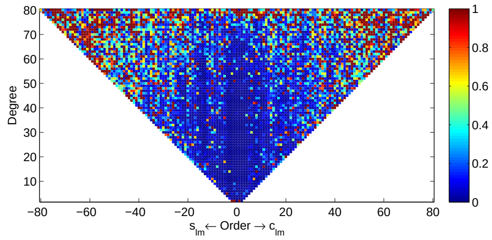

(d) Orbit 4

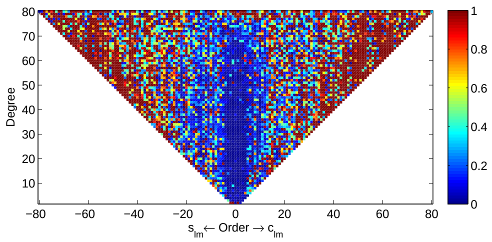

(e) Orbit 5

Figure 5.12: *REE of GRAIL 160-80 range fixed simulation*

Here the weight matrix factors are listed (table 5.8):

Table 5.8: *Documentary of weight factors*

Observation	Factor
Orbit 1	10^3
Orbit 2	10^3
Orbit 3	10^4
Orbit 4	10^7
Orbit 5	10^9

(2) 160-80 orbit fixed simulation scenario

For simplification, the along-track, cross-track and radial directions are replaced by x, y and z directions. Since the orbit accuracy in the radial direction is much better than that in the other two directions, the white noises simulated for x, y and z directions are different (table 5.9).

Table 5.9: *Simulated white noise*

Observation	White noise
Orbit	$10\ m\ (x)$ $10\ m\ (y)$ $2\ m\ (z)$
Range 1	$1\ \mu m$
Range 2	$1\ mm$
Range 3	$1\ cm$
Range 4	$10\ cm$
Range 5	$1\ m$

In figure 5.13, the raising white noises of the range measurements slightly influence the results. The solutions for range 1 to range 3 almost overlap with each other and have unconspicuous difference from the solution for range 4. Only white noise of up to 1 m leads to an obvious impact. However, 1 m is an accuracy that the KBR measurements can definitely achieve. Therefore, the effect from the range accuracy is relatively small compared to that from the orbit.

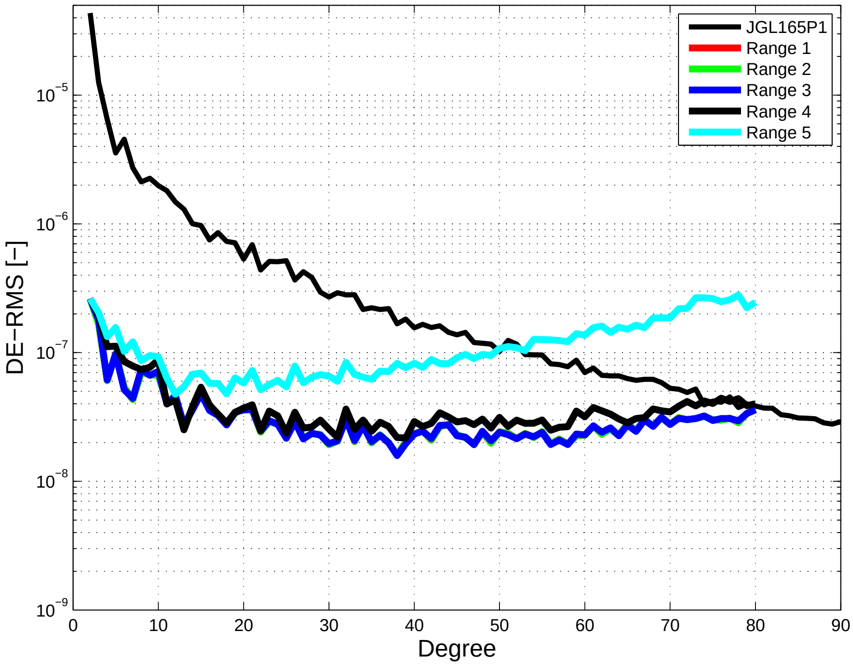

Figure 5.13: *DE-RMS of GRAIL 160-80 orbit fixed simulation*

The REE in figure 5.14 demonstrate that different range accuracies affect not only the sectorial and tesseral coefficients but also the zonal coefficients. This is because the white noises added to the range measurements influence every measurement which covers the global area.

The weight matrix factors are listed in table 5.10:

Table 5.10: *Documentary of weight factors*

Observation	Factor
Range 1	10^3
Range 2	10^3
Range 3	10^3
Range 4	1
Range 5	1

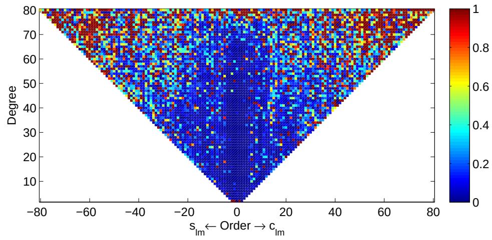

(a) Range 1

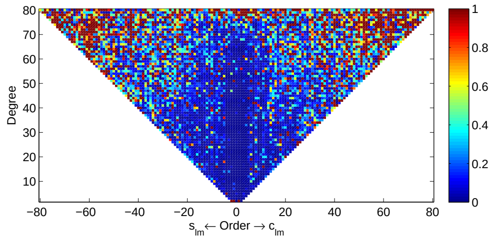

(b) Range 2

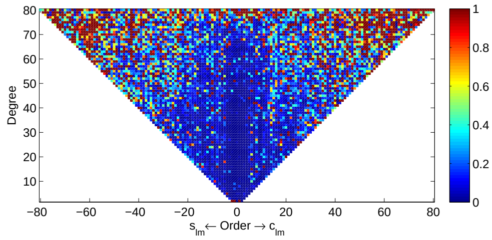

(c) Range 3

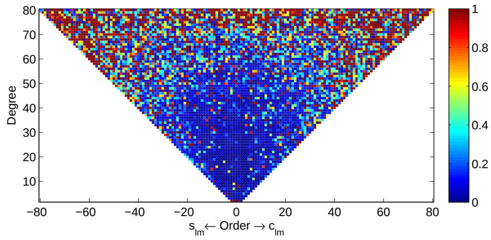

(d) Range 4

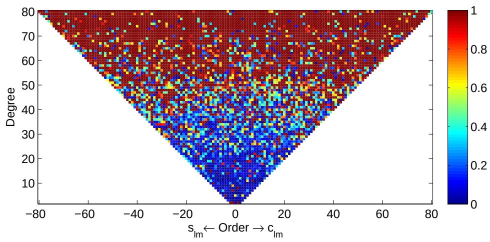

(e) Range 5

Figure 5.14: *REE of GRAIL 160-80 orbit fixed simulation*

(3) Full potential of the resolution

In order to figure out the full potential of the resolution, the tests have been undertaken with two different orbits. The simulated white noises are listed in table 5.11:

Table 5.11: *Simulated white noise*

Observation	White noise
Orbit 1	3 cm
Orbit 2	10 m (x) 10 m (y) 2 m (z)
Range	1 μm

For orbit 1, there are two resolutions under the 160-100 and 160-120 simulation scenarios respectively (figure 5.15). The DE-RMS signals of these resolutions intersect with the reference signal at degree 100 and 120 which are the maximum degrees of the reference fields. It indicates that these two resolutions still don't achieve the full potential yet. The full potential of the resolution for orbit 1 is higher than degree 120.

For orbit 2, the maximum potential of the resolution is obtained around degree 80 where the DE-RMS signals cross the reference signal under the 160-100 and 160-120 simulation scenarios. Therefore, the full potential of the resolution is limited to the orbit accuracy for the GRAIL mission.

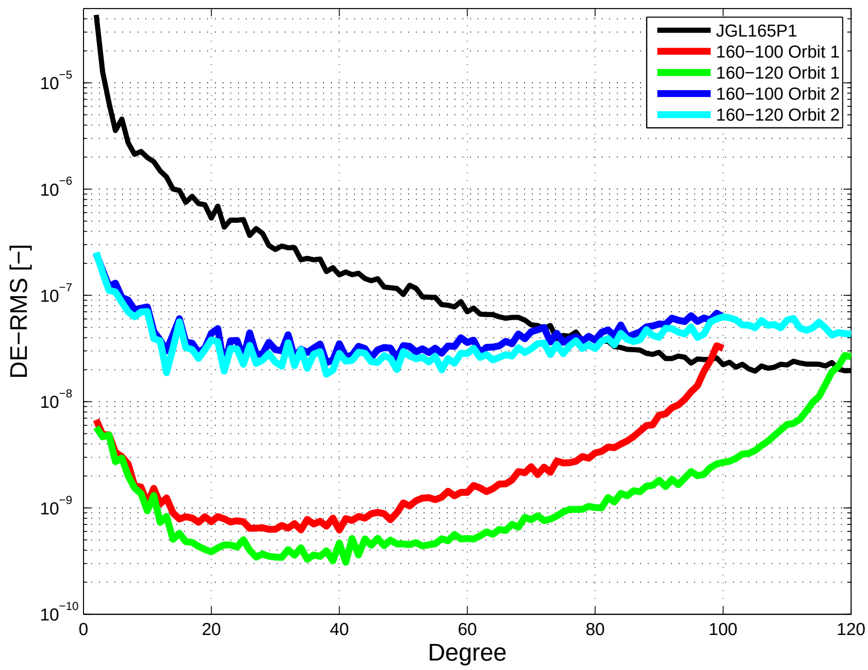

Figure 5.15: *DE-RMS of GRAIL 160 -100 and 160-120 simulation*

Chapter 6

Summary and conclusions

The prime objective of the thesis is to assess the GRAIL performance by means of a series simulation studies. It has been achieved by dividing the research into three steps:

1. The mathematical model of the short-arc approach has been set up and the modified observation equation was proposed.

2. The gravity field parameters have been estimated from the simulated GRACE and GRAIL data under different scenarios.

3. Quality assessment has been undertaken for GRAIL gravity field determination from the orbit fixed and range fixed simulation scenarios.

The conclusions are drawn as follows:

1. The short-arc approach in ll-SST model depends on the orbits and the KBR measurements. Based on the numerical integration of the variational equations, the method requires a high computational effort. Compared with the energy balance approach and the acceleration approach, it avoids combining the highly precise KBR measurements with the comparably low accurate orbits in one equation which is one of the advantages.

2. There are several solutions to improve the quality of the result from mathematical view. In the research the weight factors and arc length were chose from the empirical experience. In this way, there may exist better choices for the factors and arc length. Another solution is to introduce the arc-wise weight matrix. More iterations will not lead to an obvious improvement since the mathematical model is good enough and the observation noise is the limiting factor.

3. The relative accuracy between the orbits and the KBR measurements has a significant influence on the result. For the GRAIL mission, the result is not limited to the accuracies of the KBR measurements but limited to the accuracies of the orbits. Therefore, orbit accuracy improvement is one of the key problems, especially for the farside orbit determination.

4. Although the GRAIL mission has comparably low accurate orbits, it will still provide the best lunar gravity field ever due to the realization of the ll-SST principle for the first time.

List of Abbreviations

BVP	Boundary Value Problem
CCAFS	Cape Canaveral Air Force Station
CIS	Conventional Inertial reference System
CRS	Celestial Reference Systems
CTS	Conventional Terrestrial reference System
DE-RMS	Degree Root Mean Square
DSN	Deep Space Network
E/PO	Education/Public Outreach
GAST	Greenwich Apparent Sidereal Time
GPS	Global Positioning System
GRACE	Gravity Recovery And Climate Experiment
GRAIL	Gravity Recovery And Interior Laboratory
JPL	Jet Propulsion Laboratory
KBR	K-Band Ranging system
LGRS	Lunar Gravity Ranging System
LL-SST	Low-Low Satellite to Satellite Tracking
LM	Lockheed Martin space systems
LOI	Lunar Orbit Insertion
LOS	Line-Of-Sight
LP	Lunar Prospector
LRO	Lunar Reconnaissance Orbiter
MIT	Massachusetts Institute of Technology
NASA	National Aeronautics and Space Administration
OPR	Orbit Period Reduction
PDE	Partial Differential Equation
POD	Precision Orbit Determination
RAM	Random Access Memory
REE	Relative Empirical Errors
RSB	Ratio Science Beacon
SELENE	Selenological and Engineering Explorer
TLC	Trans-Lunar Cruise
TSF	Transition to Science Formation
TTS	Time Transfer System
USO	Ultra-Stable Oscillator

Bibliography

Akim, E. L. (1967), 'Determination of the Gravitational Field of the Moon from the Motion of the Artificial Lunar Satellite "Luna-10"', *Soviet Physics Doklady* **11**, 855.

Austen, G. and Grafarend, E. W. (2004), Gravitational field recovery from GRACE data of type high-low and low-low SST, *in* 'Proceedings of the First Joint CHAMP/-GRACE Science Team Meeting', GFZ Potsdam, Germany.

Baur, O. (2007), Die Invariantendarstellung in der Satellitengradiometrie, PhD thesis, Universität Stuttgart.

Beerer, J. G. and Havens, G. G. (2012), Operating the Dual-Orbiter GRAIL Mission to Measure the Moon's Gravity, SpaceOps 2012, Stockholm, Sweden.

Chin, G., Brylow, S., Foote, M., Garvin, J., Kasper, J., Keller, J., Litvak, M., Mitrofanov, I., Paige, D., Raney, K., Robinson, M., Sanin, A., Smith, D., Spence, H., Spudis, P., Stern, S. and Zuber, M. (2007), 'Lunar Reconnaissance Orbiter Overview: The Instrument Suite and Mission', *Space Science Reviews* **129**, 391–419.

Floberghagen, R. (2001), The Far Side: Lunar Gravimetry into the Third Millenium, Doctoral thesis, TU Delft.

Floberghagen, R. (2002), *Lunar Gravimetry*, Vol. 273, Kluwer Academic Publishers, Dordrecht, The Netherlands.

Floberghagen, R., Noomen, R., Visser, P. and Racca, G. (1996), 'Global lunar gravity recovery from satellite-to-satellite tracking', *Planetary and Space Science* **44**, 1081–1097.

Goswami, J. N. and Annadurai, M. (2009), Chandrayaan-1: India's first planetary science mission to the moon, *in* 'Lunar and Planetary Institute Science Conference Abstracts', Vol. 40 of *Lunar and Planetary Inst. Technical Report*, Woodlands, Texas, p. 2571.

Han, S.-C. (2003), Efficient global gravity determination from satellite-to-satellite tracking (SST), PhD thesis, Department of Geodetic Science, The Ohio State University, Columbus.

Havens, G. G. and Beerer, J. G. (2012), Designing Mission Operations for the Gravity Recovery and Interior Laboratory Mission, SpaceOps 2012, Stockholm, Sweden.

Heiskanen, W. and Moritz, H. (1967), 'Physical geodesy', *Bulletin géodésique* **86**, 491–492.

Hoffman, T., Bell, C. and Price, H. (2010), Systematic reliability improvements on the GRAIL project, *in* 'Aerospace Conference, 2010 IEEE', pp. 1 –12.

Jekeli, C. (1999), 'The determination of gravitational potential differences from satellite-to-satellite tracking', *Celestial Mechanics and Dynamical Astronomy* **75**, 85–101.

Kaula, W. (1966), *Theory of Satellite Geodesy, Applications of Satellites to Geodesy*, Blaisdell Publishing Company.

Keller, W. and Sharifi, M. (2005), 'Satellite gradiometry using a satellite pair', *Journal of Geodesy* **78**, 544–557.

Konopliv, A., Asmar, S., Carranza, E., Sjogren, W. and Yuan, D. (2001), 'Recent Gravity Models as a Result of the Lunar Prospector Mission', *Icarus* **150**, 1–18.

Lemoine, F. G., Kenyon, S. C., Factor, J. K., Trimmer, R. G., Pavlis, N. K., Chinn, D. S., Cox, C. M., Klosko, S. M., Luthcke, S. B., Torrence, M. H., Wang, Y. M., Williamson, R. G., Pavlis, E. C. and Rapp, R. H. (1998), *The development of the joint NASA GSFC and the National Imagery and Mapping Agency (NIMA) Geopotential Model EGM96*, NASA Goddard Space Flight Cent., Greenbelt, Md.

Lemoine, F. G. R., Smith, D. E., Zuber, M. T., Neumann, G. A. and Rowlands, D. D. (1997), 'A 70th degree lunar gravity model (GLGM-2) from Clementine and other tracking data', *J. Geophys. Res.* **102**(E7), 16,339C16,359.

Liu, X. (2008), Global gravity field recovery from satellite-to-satellite tracking data with the acceleration approach, PhD thesis, Delft University of Technology.

Mayer-Gürr, T. (2006), Gravitationsfeldbestimmung aus der Analyse kurzer Bahnbögen am Beispiel der Satellitenmissionen CHAMP und GRACE, PhD thesis, Universität Bonn.

Mayer-Gürr, T., Ilk, K., Eicker, A. and Feuchtinger, M. (2005), 'ITG-CHAMP01: a CHAMP gravity field model from short kinematic arcs over a one-year observation period', *Journal of Geodesy* **78**, 462–480.

Mayer-Gürr, T., Ilk, K.-H. andFeuchtinger, M. and Eicker, A. (2004), Global and Regional Gravity Field Solutions from GRACE Observations, Proceedings of the Joint CHAMP/GRACE Science Meeting, GeoForschungsZentrum Potsdam.

Mazarico, E., Rowlands, D., Neumann, G., Smith, D., Torrence, M., Lemoine, F. and Zuber, M. (2012), 'Orbit determination of the Lunar Reconnaissance Orbiter', *Journal of Geodesy* **86**, 193–207.

Muller, P. M. and Sjogren, W. L. (1968), 'Mascons: Lunar mass concentrations', *Science* **161**, 680–684.

Namiki, N., Iwata, T., Matsumoto, K., Hanada, H., Noda, H., Goossens, S., Ogawa, M., Kawano, N., Asari, K., itsu Tsuruta, S., Ishihara, Y., Liu, Q., Kikuchi, F., Ishikawa, T., Sasaki, S., Aoshima, C., Kurosawa, K., Sugita, S., and Takano, T. (2009), 'Farside Gravity Field of the Moon from Four-Way Doppler Measurements of SE-

LENE (Kaguya)’, *Science* **323**(5916), 900–905.

NASA (2011), ‘Gravity Recovery and Interior Laboratory (GRAIL) Launch’, Press Kit, National Aeronautics and Space Administration.

Novák, P., Austen, G., Sharifi, M. and Grafarend, E. (2006), Mapping Earth’s Gravitation Using GRACE Data, *in* J. Flury, R. Rummel, C. Reigber, M. Rothacher, G. Boedecker and U. Schreiber, eds, ‘Observation of the Earth System from Space’, Springer Berlin Heidelberg, pp. 149–164.

Petit, G. and Luzum, B. (2010), IERS Conventions (2010), Technical report, Frankfurt am Main: Verlag des Bundesamts für Kartographie und Geodäsie.

Reigber, C. (1989), Gravity field recovery from satellite tracking data, *in* F. Sansò and R. Rummel, eds, ‘Theory of Satellite Geodesy and Gravity Field Determination’, Vol. 25 of *Lecture Notes in Earth Sciences*, Springer Berlin Heidelberg, pp. 197–234.

Reigber, C., Schmidt, R., Flechtner, F., König, R., Meyer, U., Neumayer, K.-H., Schwintzer, P. and Zhu, S. Y. (2005), ‘An Earth gravity field model complete to degree and order 150 from GRACE: EIGEN-GRACE02S’, *Journal of Geodynamics* **39**(1), 1–10.

Reubelt, T., Austen, G. and Grafarend, E. (2003), ‘Harmonic analysis of the Earth’s gravitational field by means of semi-continuous ephemerides of a low Earth orbiting GPS-tracked satellite. Case study: CHAMP’, *Journal of Geodesy* **77**, 257–278.

Reubelt, T., Götzelmann, M. and Grafarend, E. (2006), Harmonic Analysis of the Earth’s Gravitational Field from Kinematic CHAMP Orbits based on Numerically Derived Satellite Accelerations, *in* J. Flury, R. Rummel, C. Reigber, M. Rothacher, G. Boedecker and U. Schreiber, eds, ‘Observation of the Earth System from Space’, Springer Berlin Heidelberg, pp. 27–42.

Ries, J. C., Cheng, M., Bettadpur, S. and Chambers, D. P. (2008), SLR-determined Low-Degree Geopotential Harmonics and their use With GRACE Data Products, American Geophysical Union.

Schneider, M. (1968), ‘A general method of orbit determination’, Technical Report, NASA.

Seeber, G. (2003), *Satellite Geodesy*, Institut für Erdmessung, Universität Hannover.

Sneeuw, N. (2006), Physical Geodesy, Lecture notes, Geodätisches Institut, Universität Stuttgart.

Tapley, B. D., Bettadpur, S., Watkins, M. and Reigber, C. (2004), ‘The gravity recovery and climate experiment: Mission overview and early results’, *Geophysical Research Letters* **31**(L09607), 4.

Vondrak, R., Keller, J., Chin, G. and Garvin, J. (2010), ‘Lunar Reconnaissance Orbiter (LRO): Observations for Lunar Exploration and Science’, *Space Science Reviews* **150**, 7–22.

Wang, R. and Klipstein, W. (2010), GRAIL-A microwave ranging instrument to map out the lunar gravity field, *in* 'Frequency Control Symposium (FCS), 2010 IEEE International', Jet Propulsion Lab., California Inst. of Technol., Pasadena, CA, USA, pp. 572–577.

Weigelt, M. and Keller, W. (2011), GRACE Gravity Field Solutions Using the Differential Gravimetry Approach, *in* 'IUGG General Assembly - Earth on the Edge: Science for a Sustainable Planet', Melbourne, Australia.

Weigelt, M. L. (2007), Global and local gravity field recovery from satellite-to-satellite tracking, PhD thesis, University of Calgary.

Yan, J., Ping, J., Li, F., Cao, J., Huang, Q. and Fung, L. (2010), 'Chang'E-1 precision orbit determination and lunar gravity field solution', *Advances in Space Research* **46**, 50–57.

Zuber, M. (2008), GRAIL Gravity Mission: Goals and Status, *in* '37th COSPAR Scientific Assembly', in Montréal, Canada.

Appendix A

Gravity gradient calculation

For the calculation of the elements in equation 4.32:

$$\mathbf{T} = \begin{pmatrix} \nabla \mathbf{f}(\tau_1) & & 0 \\ & \ddots & \\ 0 & & \nabla \mathbf{f}(\tau_N) \end{pmatrix} \tag{A.1}$$

The elements are denoted as:

$$\nabla \mathbf{f}(\tau) = \begin{pmatrix} V_{XX} & V_{XY} & V_{XZ} \\ V_{YX} & V_{YY} & V_{YZ} \\ V_{ZX} & V_{ZY} & V_{ZZ} \end{pmatrix} \tag{A.2}$$

$$\begin{aligned} V_{\lambda\lambda} = \frac{\partial^2 V}{\partial \lambda^2} = \frac{GM}{R^3} \sum_{l=0}^{L} \sum_{m=0}^{l} (\frac{R}{r})^{l+3} [-(l+1)\bar{P}_{lm}(\sin\theta) - m^2 \frac{1}{\cos^2\varphi} \bar{P}_{lm}(\sin\theta) \\ - \tan\varphi \frac{\partial \bar{P}_{lm}(\sin\theta)}{\partial \varphi}](\bar{C}_{lm}\cos m\lambda + \bar{S}_{lm}\sin m\lambda) \end{aligned} \tag{A.3}$$

$$\begin{aligned} V_{\varphi\varphi} = \frac{\partial^2 V}{\partial \varphi^2} = \frac{GM}{R^3} \sum_{l=0}^{L} \sum_{m=0}^{l} (\frac{R}{r})^{l+3} [-(l+1)\bar{P}_{lm}(\sin\theta) + \frac{\partial^2 \bar{P}_{lm}(\sin\theta)}{\partial \varphi^2}] \\ (\bar{C}_{lm}\cos m\lambda + \bar{S}_{lm}\sin m\lambda) \end{aligned} \tag{A.4}$$

$$\begin{aligned} V_{rr} = \frac{\partial^2 V}{\partial r^2} = \frac{GM}{R^3} \sum_{l=0}^{L} \sum_{m=0}^{l} (\frac{R}{r})^{l+3} (l+1)(l+2)\bar{P}_{lm}(\sin\theta)(\bar{C}_{lm}\cos m\lambda + \\ \bar{S}_{lm}\sin m\lambda) \end{aligned} \tag{A.5}$$

$$\begin{aligned} V_{\lambda\varphi} = \frac{\partial^2 V}{\partial \lambda \partial \varphi} = \frac{GM}{R^3} \sum_{l=0}^{L} \sum_{m=0}^{l} (\frac{R}{r})^{l+3} [-\tan\varphi \bar{P}_{lm}(\sin\theta) - \frac{\partial \bar{P}_{lm}(\sin\theta)}{\partial \varphi}] \frac{m}{\cos\varphi} \\ (\bar{C}_{lm}\sin m\lambda - \bar{S}_{lm}\cos m\lambda) \end{aligned} \tag{A.6}$$

$$V_{\lambda r} = \frac{\partial^2 V}{\partial\lambda\partial r} = \frac{GM}{R^3}\sum_{l=0}^{L}\sum_{m=0}^{l}(\frac{R}{r})^{l+3}(l+2)\frac{m}{\cos\varphi}\bar{P}_{lm}(\sin\theta)(\bar{C}_{lm}\sin m\lambda - \bar{S}_{lm}\cos m\lambda) \tag{A.7}$$

$$V_{\varphi r} = \frac{\partial^2 V}{\partial\varphi\partial r} = \frac{GM}{R^3}\sum_{l=0}^{L}\sum_{m=0}^{l}(\frac{R}{r})^{l+3}[-(l+2)\frac{\partial\bar{P}_{lm}(\sin\theta)}{\partial\varphi}(\bar{C}_{lm}\cos m\lambda + \bar{S}_{lm}\sin m\lambda) \tag{A.8}$$

where $V_{XX} = V_{\lambda\lambda}$, $V_{YY} = V_{\varphi\varphi}$, $V_{ZZ} = V_{rr}$.

Appendix B

Arrangement of the matrices

There are two ways to arrange the matrices in section 4.4.1. Sorting by time means to arrange the elements at same epochs together whereas sorting by direction means to arrange the elements in the same directions together.

B.1 Sorting by time

$$\kappa = T^2 \int_0^1 K(\tau, \tau')(\cdot) d\tau' \tag{B.1}$$

$$\mathbf{K} = \begin{bmatrix} b_1^{\tau_1} & 0 & 0 & & & b_n^{\tau_1} & 0 & 0 \\ 0 & b_1^{\tau_1} & 0 & \dots & \dots & 0 & b_n^{\tau_1} & 0 \\ 0 & 0 & b_1^{\tau_1} & & & 0 & 0 & b_n^{\tau_1} \\ b_1^{\tau_2} & 0 & 0 & & & b_n^{\tau_2} & 0 & 0 \\ 0 & b_1^{\tau_2} & 0 & \dots & \dots & 0 & b_n^{\tau_2} & 0 \\ 0 & 0 & b_1^{\tau_2} & & & 0 & 0 & b_n^{\tau_2} \\ \vdots & \vdots & \vdots & & & \vdots & \vdots & \vdots \\ b_1^{\tau_n} & 0 & 0 & & & b_n^{\tau_n} & 0 & 0 \\ 0 & b_1^{\tau_n} & 0 & \dots & \dots & 0 & b_n^{\tau_n} & 0 \\ 0 & 0 & b_1^{\tau_n} & & & 0 & 0 & b_n^{\tau_n} \end{bmatrix}$$

$$\mathbf{B} = \begin{bmatrix} 1-\tau_1 & 0 & 0 & \tau_1 & 0 & 0 \\ 0 & 1-\tau_1 & 0 & 0 & \tau_1 & 0 \\ 0 & 0 & 1-\tau_1 & 0 & 0 & \tau_1 \\ 1-\tau_2 & 0 & 0 & \tau_2 & 0 & 0 \\ 0 & 1-\tau_2 & 0 & 0 & \tau_2 & 0 \\ 0 & 0 & 1-\tau_2 & 0 & 0 & \tau_2 \\ \vdots & \vdots & \vdots & \vdots & \vdots & \vdots \\ 1-\tau_n & 0 & 0 & \tau_n & 0 & 0 \\ 0 & 1-\tau_n & 0 & 0 & \tau_n & 0 \\ 0 & 0 & 1-\tau_n & 0 & 0 & \tau_n \end{bmatrix} \tag{B.2}$$

$$\dot{\mathbf{B}} = \frac{1}{T}\begin{bmatrix} -1 & 0 & 0 & 1 & 0 & 0 \\ 0 & -1 & 0 & 0 & 1 & 0 \\ 0 & 0 & -1 & 0 & 0 & 1 \\ -1 & 0 & 0 & 1 & 0 & 0 \\ 0 & -1 & 0 & 0 & 1 & 0 \\ 0 & 0 & -1 & 0 & 0 & 1 \\ \vdots & \vdots & \vdots & \vdots & \vdots & \vdots \\ -1 & 0 & 0 & 1 & 0 & 0 \\ 0 & -1 & 0 & 0 & 1 & 0 \\ 0 & 0 & -1 & 0 & 0 & 1 \end{bmatrix} \tag{B.3}$$

$$\mathbf{T} = \begin{bmatrix} \begin{bmatrix} T_{xx} & T_{xy} & T_{xz} \\ T_{yx} & T_{yy} & T_{yz} \\ T_{zx} & T_{zy} & T_{zz} \end{bmatrix} (\tau_1) & & & \\ & \begin{bmatrix} T_{xx} & T_{xy} & T_{xz} \\ T_{yx} & T_{yy} & T_{yz} \\ T_{zx} & T_{zy} & T_{zz} \end{bmatrix} (\tau_2) & & \\ & & \ddots & \\ & & & \begin{bmatrix} T_{xx} & T_{xy} & T_{xz} \\ T_{yx} & T_{yy} & T_{yz} \\ T_{zx} & T_{zy} & T_{zz} \end{bmatrix} (\tau_n) \end{bmatrix} \tag{B.4}$$

$$\mathbf{r} - \hat{\mathbf{r}} = \kappa \nabla \mathbf{f}(\mathbf{r} - \mathbf{r}_{\varepsilon}) \tag{B.5}$$

$$\begin{bmatrix} \begin{bmatrix} \Delta x \\ \Delta y \\ \Delta z \end{bmatrix} (\tau_1) \\ \begin{bmatrix} \Delta x \\ \Delta y \\ \Delta z \end{bmatrix} (\tau_2) \\ \vdots \\ \begin{bmatrix} \Delta x \\ \Delta y \\ \Delta z \end{bmatrix} (\tau_n) \end{bmatrix} = \mathbf{K}_{3N\times 3N}\mathbf{T}_{3N\times 3N} \begin{bmatrix} \begin{bmatrix} \Delta x' \\ \Delta y' \\ \Delta z' \end{bmatrix} (\tau_1) \\ \begin{bmatrix} \Delta x' \\ \Delta y' \\ \Delta z' \end{bmatrix} (\tau_2) \\ \vdots \\ \begin{bmatrix} \Delta x' \\ \Delta y' \\ \Delta z' \end{bmatrix} (\tau_n) \end{bmatrix}_{3N\times 1}$$

$$\Delta\mathbf{r} = (\mathbf{I} - \mathbf{KT})^{-1}(\mathbf{Kf} + \mathbf{Bb} - \mathbf{r}_{\varepsilon}) \tag{B.6}$$

$$\Delta\mathbf{r} = \begin{bmatrix} \begin{bmatrix} \Delta x \\ \Delta y \\ \Delta z \end{bmatrix} (\tau_1) \\ \begin{bmatrix} \Delta x \\ \Delta y \\ \Delta z \end{bmatrix} (\tau_2) \\ \vdots \\ \begin{bmatrix} \Delta x \\ \Delta y \\ \Delta z \end{bmatrix} (\tau_n) \end{bmatrix} = (\mathbf{I} - \mathbf{KT})^{-1}(\mathbf{K} \begin{bmatrix} \begin{bmatrix} f_x \\ f_y \\ f_z \end{bmatrix} (\tau_1) \\ \begin{bmatrix} f_x \\ f_y \\ f_z \end{bmatrix} (\tau_2) \\ \vdots \\ \begin{bmatrix} f_x \\ f_y \\ f_z \end{bmatrix} (\tau_n) \end{bmatrix} + \mathbf{B} \begin{bmatrix} r_x^A \\ r_y^A \\ r_z^A \\ r_x^B \\ r_y^B \\ r_z^B \end{bmatrix} - \begin{bmatrix} \begin{bmatrix} x \\ y \\ z \end{bmatrix} (\tau_1) \\ \begin{bmatrix} x \\ y \\ z \end{bmatrix} (\tau_2) \\ \vdots \\ \begin{bmatrix} x \\ y \\ z \end{bmatrix} (\tau_n) \end{bmatrix})$$

B.2 Sorting by direction

$$\kappa = T^2 \int_0^1 K(\tau, \tau')(\cdot) d\tau' \tag{B.7}$$

$$\mathbf{K}_T = \begin{bmatrix} b_1^{\tau_1} & b_2^{\tau_1} & \dots & b_n^{\tau_1} \\ b_1^{\tau_2} & b_2^{\tau_2} & \dots & b_n^{\tau_2} \\ \vdots & \vdots & \ddots & \vdots \\ b_1^{\tau_n} & b_2^{\tau_n} & \dots & b_n^{\tau_n} \end{bmatrix}_{3N \times 3N}$$

$$\mathbf{B}_T = \begin{bmatrix} 1-\tau_1 & \tau_1 \\ \vdots & \vdots \\ 1-\tau_n & \tau_n \end{bmatrix} \tag{B.8}$$

$$\dot{\mathbf{B}}_T = \frac{1}{T} \begin{bmatrix} -1 & 1 \\ \vdots & \vdots \\ -1 & 1 \end{bmatrix} \tag{B.9}$$

$$\mathbf{T}_T = \begin{bmatrix} \begin{bmatrix} T_{xx}^{\tau_1} & & \\ & \ddots & \\ & & T_{xx}^{\tau_n} \end{bmatrix} & \begin{bmatrix} T_{xy}^{\tau_1} & & \\ & \ddots & \\ & & T_{xy}^{\tau_n} \end{bmatrix} & \begin{bmatrix} T_{xz}^{\tau_1} & & \\ & \ddots & \\ & & T_{xz}^{\tau_n} \end{bmatrix} \\ \begin{bmatrix} T_{yx}^{\tau_1} & & \\ & \ddots & \\ & & T_{yx}^{\tau_n} \end{bmatrix} & \begin{bmatrix} T_{yy}^{\tau_1} & & \\ & \ddots & \\ & & T_{yy}^{\tau_n} \end{bmatrix} & \begin{bmatrix} T_{yz}^{\tau_1} & & \\ & \ddots & \\ & & T_{yz}^{\tau_n} \end{bmatrix} \\ \begin{bmatrix} T_{zx}^{\tau_1} & & \\ & \ddots & \\ & & T_{zx}^{\tau_n} \end{bmatrix} & \begin{bmatrix} T_{zy}^{\tau_1} & & \\ & \ddots & \\ & & T_{zy}^{\tau_n} \end{bmatrix} & \begin{bmatrix} T_{zz}^{\tau_1} & & \\ & \ddots & \\ & & T_{zz}^{\tau_n} \end{bmatrix} \end{bmatrix} \tag{B.10}$$

$$\mathbf{r} - \hat{\mathbf{r}} = \kappa \nabla \mathbf{f}(\mathbf{r} - \mathbf{r}_{\varepsilon}) \tag{B.11}$$

$$\begin{bmatrix} \Delta x(\tau_1) \\ \Delta x(\tau_2) \\ \vdots \\ \Delta x(\tau_n) \\ \Delta y(\tau_1) \\ \vdots \\ \Delta y(\tau_n) \\ \Delta z(\tau_1) \\ \vdots \\ \Delta z(\tau_n) \end{bmatrix} = \begin{bmatrix} \mathbf{K}_T & & \\ & \mathbf{K}_T & \\ & & \mathbf{K}_T \end{bmatrix}_{3N \times 3N} \mathbf{T}_{T3N \times 3N} \begin{bmatrix} \Delta x'(\tau_1) \\ \Delta x'(\tau_2) \\ \vdots \\ \Delta x'(\tau_n) \\ \Delta y'(\tau_1) \\ \vdots \\ \Delta y'(\tau_n) \\ \Delta z'(\tau_1) \\ \vdots \\ \Delta z'(\tau_n) \end{bmatrix}_{3N \times 1}$$

$$\Delta \mathbf{r} = (\mathbf{I} - \mathbf{K}\mathbf{T})^{-1}(\mathbf{K}\mathbf{f} + \mathbf{B}\mathbf{b} - \mathbf{r}_{\varepsilon}) \tag{B.12}$$

$$\Delta \mathbf{r} = \begin{bmatrix} \Delta x(\tau_1) \\ \Delta x(\tau_2) \\ \vdots \\ \Delta x(\tau_n) \\ \Delta y(\tau_1) \\ \vdots \\ \Delta y(\tau_n) \\ \Delta z(\tau_1) \\ \vdots \\ \Delta z(\tau_n) \end{bmatrix} = (\mathbf{I} - \begin{bmatrix} \mathbf{K}_T \begin{bmatrix} T_{xx}^{\tau_1} & & \\ & \ddots & \\ & & T_{xx}^{\tau_n} \end{bmatrix} & \mathbf{K}_T \begin{bmatrix} T_{xy}^{\tau_1} & & \\ & \ddots & \\ & & T_{xy}^{\tau_n} \end{bmatrix} & \mathbf{K}_T \begin{bmatrix} T_{xz}^{\tau_1} & & \\ & \ddots & \\ & & T_{xz}^{\tau_n} \end{bmatrix} \\ \mathbf{K}_T \begin{bmatrix} T_{yx}^{\tau_1} & & \\ & \ddots & \\ & & T_{yx}^{\tau_n} \end{bmatrix} & \mathbf{K}_T \begin{bmatrix} T_{yy}^{\tau_1} & & \\ & \ddots & \\ & & T_{yy}^{\tau_n} \end{bmatrix} & \mathbf{K}_T \begin{bmatrix} T_{yz}^{\tau_1} & & \\ & \ddots & \\ & & T_{yz}^{\tau_n} \end{bmatrix} \\ \mathbf{K}_T \begin{bmatrix} T_{zx}^{\tau_1} & & \\ & \ddots & \\ & & T_{zx}^{\tau_n} \end{bmatrix} & \mathbf{K}_T \begin{bmatrix} T_{zy}^{\tau_1} & & \\ & \ddots & \\ & & T_{zy}^{\tau_n} \end{bmatrix} & \mathbf{K}_T \begin{bmatrix} T_{zz}^{\tau_1} & & \\ & \ddots & \\ & & T_{zz}^{\tau_n} \end{bmatrix} \end{bmatrix})^{-1}$$

$$\left(\begin{bmatrix} \mathbf{K}_T \begin{bmatrix} f_x(\tau_1) \\ \vdots \\ f_x(\tau_n) \end{bmatrix} \\ \mathbf{K}_T \begin{bmatrix} f_y(\tau_1) \\ \vdots \\ f_y(\tau_n) \end{bmatrix} \\ \mathbf{K}_T \begin{bmatrix} f_z(\tau_1) \\ \vdots \\ f_z(\tau_n) \end{bmatrix} \end{bmatrix} + \begin{bmatrix} \mathbf{B}_T \begin{bmatrix} r_x^A \\ r_x^B \end{bmatrix} \\ \mathbf{B}_T \begin{bmatrix} r_y^A \\ r_y^B \end{bmatrix} \\ \mathbf{B}_T \begin{bmatrix} r_z^A \\ r_z^B \end{bmatrix} \end{bmatrix} - \begin{bmatrix} x(\tau_1) \\ x(\tau_2) \\ \vdots \\ x(\tau_n) \\ y(\tau_1) \\ \vdots \\ y(\tau_n) \\ z(\tau_1) \\ \vdots \\ z(\tau_n) \end{bmatrix} \right)$$

$$\mathbf{R}^{A/B} = \frac{\partial \mathbf{r}}{\partial \mathbf{f}}^{A/B} = (\mathbf{I} - \mathbf{K}\mathbf{T}^{A/B})^{-1}\mathbf{K} \tag{B.13}$$

$$\bar{\mathbf{B}}^{A/B} = \frac{\partial \mathbf{r}}{\partial \mathbf{b}}^{A/B} = (\mathbf{I} - \mathbf{K}\mathbf{T}^{A/B})^{-1}\mathbf{B} \tag{B.14}$$

$$\mathbf{R}^{A/B} = (\mathbf{I} - \mathbf{K}\mathbf{T}^{A/B})^{-1}_{3N\times 3N} \begin{bmatrix} \mathbf{K}_T & & \\ & \mathbf{K}_T & \\ & & \mathbf{K}_T \end{bmatrix}_{3N\times 3N}$$

$$\bar{\mathbf{B}}^{A/B} = (\mathbf{I} - \mathbf{K}\mathbf{T}^{A/B})^{-1}_{3N\times 3N} \begin{bmatrix} \mathbf{B}_T & & \\ & \mathbf{B}_T & \\ & & \mathbf{B}_T \end{bmatrix}_{3N\times 3N}$$

$$\dot{\mathbf{R}}^{A/B} = \frac{\partial \dot{\mathbf{r}}}{\partial \mathbf{f}}^{A/B} = \dot{\mathbf{K}}\ddot{\mathbf{R}}^{A/B} \tag{B.15}$$

$$\dot{\mathbf{B}}^{A/B} = \frac{\partial \dot{\mathbf{r}}}{\partial \mathbf{b}}^{A/B} = \dot{\mathbf{B}} + \dot{\mathbf{K}}\ddot{\mathbf{B}}^{A/B} \tag{B.16}$$

$$\dot{\mathbf{R}}^{A/B} = \begin{bmatrix} \dot{\mathbf{K}}_T & & \\ & \dot{\mathbf{K}}_T & \\ & & \dot{\mathbf{K}}_T \end{bmatrix} \ddot{\mathbf{R}}^{A/B}$$

$$\dot{\mathbf{B}}^{A/B} = \begin{bmatrix} \dot{\mathbf{B}}_T & & \\ & \dot{\mathbf{B}}_T & \\ & & \dot{\mathbf{B}}_T \end{bmatrix} + \begin{bmatrix} \dot{\mathbf{K}}_T & & \\ & \dot{\mathbf{K}}_T & \\ & & \dot{\mathbf{K}}_T \end{bmatrix} \ddot{\mathbf{R}}^{A/B}$$

$$\ddot{\mathbf{r}}_0^{A/B} = \mathbf{f}_0^{A/B} + \mathbf{T}^{A/B}\Delta\mathbf{r}^{A/B} \tag{B.17}$$

$$\ddot{\mathbf{r}}_0^{A/B} = \begin{bmatrix} \begin{bmatrix} f_x(\tau_1) \\ \vdots \\ f_x(\tau_n) \end{bmatrix} \\ \begin{bmatrix} f_y(\tau_1) \\ \vdots \\ f_y(\tau_n) \end{bmatrix} \\ \begin{bmatrix} f_z(\tau_1) \\ \vdots \\ f_z(\tau_n) \end{bmatrix} \end{bmatrix} + \mathbf{T}_T \begin{bmatrix} \Delta x(\tau_1) \\ \Delta x(\tau_2) \\ \vdots \\ \Delta x(\tau_n) \\ \Delta y(\tau_1) \\ \vdots \\ \Delta y(\tau_n) \\ \Delta z(\tau_1) \\ \vdots \\ \Delta z(\tau_n) \end{bmatrix}$$

$$\dot{\mathbf{r}}_0^{A/B} = \dot{\mathbf{K}}\ddot{\mathbf{r}}_0^{A/B} + \dot{\mathbf{B}}\mathbf{b}_0^{A/B} \tag{B.18}$$

$$\dot{\mathbf{r}}_0^{A/B} = \begin{bmatrix} \dot{\mathbf{K}}_T & & \\ & \dot{\mathbf{K}}_T & \\ & & \dot{\mathbf{K}}_T \end{bmatrix} \begin{bmatrix} \ddot{\mathbf{r}}_0(x) \\ \ddot{\mathbf{r}}_0(y) \\ \ddot{\mathbf{r}}_0(z) \end{bmatrix} + \begin{bmatrix} \dot{\mathbf{B}}_T & & \\ & \dot{\mathbf{B}}_T & \\ & & \dot{\mathbf{B}}_T \end{bmatrix} \begin{bmatrix} \begin{bmatrix} r_x^A \\ r_x^B \end{bmatrix} \\ \begin{bmatrix} r_y^A \\ r_y^B \end{bmatrix} \\ \begin{bmatrix} r_z^A \\ r_z^B \end{bmatrix} \end{bmatrix}$$